The Hydrodynamic Design and Analysis of an RP-1 Pump for a Liquid Rocket Engine

by

Creason Chetty

Submitted in fulfilment of the academic requirements for the degree of Master of Science in Mechanical Engineering, College of Agriculture, Engineering and Science,

University of KwaZulu-Natal

Supervisor: Dr Michael Brooks

Co-supervisors: Prof. Graham Smith

Dr Glen Snedden (CSIR)

Declaration 1 - Plagiarism

I, Creason Chetty, declare that

1. The research reported in this thesis, except where otherwise indicated, is my original research.
2. This thesis has not been submitted for any degree or examination at any other university.
3. This thesis does not contain other persons' data, pictures, graphs or other information, unless specifically acknowledged as being sourced from other persons.
4. This thesis does not contain other persons' writing, unless specifically acknowledged as being sourced from other researchers. Where other written sources have been quoted, then:

a. Their words have been re-written but the general information attributed to them has been referenced
b. Where their exact words have been used, then their writing has been placed in italics and inside quotation marks, and referenced.

5. This thesis does not contain text, graphics or tables copied and pasted from the Internet, unless specifically acknowledged, and the source being detailed in the thesis and in the References sections.

Signed: .Date: .

Mr Creason Chetty

As the candidate's supervisor I have approved this dissertation for submission.

Signed: .Date: .

Dr Michael Brooks

As the candidate's co-supervisor I have approved this dissertation for submission.

Signed: .Date: .

Prof. Graham Smith

As the candidate's co-supervisor I have approved this dissertation for submission.

Signed: .Date: .

Dr Glen Snedden (CSIR)

Acknowledgements

I would like to thank my supervisors, Dr Michael Brooks and Prof. Graham Smith, for their continuous guidance and support. To my colleague and friend, Nalendran Singh, who proved to be an invaluable sounding board throughout the duration of this project. To Dr Glen Snedden and Radeshen Moodley, at the CSIR, for always being more than happy to assist with technical support and affording myself and Nalendran the opportunity to participate in the 2016, IASSA conference.

And finally I would like to thank the South African National Space Agency (SANSA) for funding this work.

Abstract

South Africa has a fledgling satellite industry but lacks the ability to launch spacecraft into low Earth orbit. As a result, the University of KwaZulu-Natal's (UKZN's) Aerospace Systems Research Group (ASReG) began the development of the South African First Integrated Rocket Engine (SAFFIRE). SAFFIRE aims to be a versatile, small scale, liquid rocket engine capable of being clustered for use on small-satellite ('small-sat') launch vehicles. The propellants for the proposed engine are Rocket Propellant-1 (RP-1) and liquid oxygen (LOX), which are fed into the combustion chamber via the injector. The uniqueness of SAFFIRE lies in the use of electrically driven pumps ('electropumps') as opposed to the conventional turbopump design. The electropump system has the fuel and oxidiser pumps independently housed and driven by brushless DC motors, which draw power from a lithium-polymer battery pack.

A hypothetical launch vehicle was proposed to validate design specifications for the SAFFIRE engine, from which the hydrodynamic requirements of the electropump system were obtained. A meanline design algorithm was developed, using conventional design methods for centrifugal pumps. The algorithm was constructed to simultaneously meet the hydrodynamic system requirements of the engine, minimize the potential of cavitation at the fuel pump inlet and maximize the operational speed to minimize the overall pump weight. The hydrodynamic requirements of the system result in a low specific speed design, thus placing the pump in the region between full emission centrifugal pumps and positive displacement pumps. The low specific speed presented unique problems, not commonly encountered via the conventional pump design method, such as excessively small blade exit widths that are sensitive to dimensional variations. The Barske pump was investigated as a potential solution; it is a partial emission pump with the meanline design being governed by vortex theory. A comparative analysis between the conventional and Barske design was done using computational fluid dynamic techniques.

The final hydrodynamic design is a hybrid between a Barske impeller and a scroll collection volute, which is typically found on a full emission pump. An investigation was done to determine an appropriate solution for mitigating the cavitation. It was found that the initial 3 bar tank pressure, suggested by literature, is applicable for an equivalent engine utilizing a turbopump system. The optimal tank pressure for the electropump system was found to be 9 bar. This increased available pressure head at the inlet of the pump eliminated any form of cavitation. The hybrid pump delivers 62.12 bar of pressure at a mass flow rate of 2.75 kg/s with a 62.12 % efficiency.

Table of Contents

List of Figures

Appendix A

Appendix C

Appendix D

List of Tables

Nomenclature

Constants

$g = 9.81$ m/s^2	Earth's gravitational acceleration
$G = 6.673\times10^{-11}$ N.m^2 /kg^2	Newton's universal gravitational constant
$R_E = 6371$ km	Radius of the Earth

Symbols

A	Area	[m^2]
AR	Area Ratio	[-]
b_2	Impeller exit width	[m]
C	Absolute velocity	[m/s]
C_θ	Tangential velocity	[m/s]
C_m	Meridional velocity	[m/s]
d	Internal pipe diameter	[m]
D	Diameter	[m]
f	Friction factor	[-]
Ft	Engine thrust	[N]
H	Head	[m]
H_{fr}	Pipe friction head loss	[m]
H_{req}	Required head rise across pump	[m]
Isp	Specific impulse	[s]
L	Chamber length	[m]
l	Tank length	[m]
l_d	Conical diffuser length	[m]

M	Mach number	[-]
m	Mass	[kg]
$\dot{m}$	Mass flow rate	[kg/s]
Mw	Molecular weight	[kg/mol]
N	Rotational speed	[rpm]
n_q	Metric specific speed	[-]
O/F	Oxidiser to fuel ratio	[-]
OA	Orbital altitude	[km]
P	Pressure	[Pa]
$P0$	Initial fuel tank pressure	[Pa]
P_v	Vapour pressure	[Pa]
Q	Flowrate	[m^3/s]
R	Specific gas constant	[J/kg.K]
r	Radius	[m]
Re	Reynolds number	[-]
s	Axial clearance	[m]
T	Temperature	[K]
Ta	Ascent time	[s]
t	Thickness	[m]
t_{day}	Time taken for a single revolution of the earth	[s]
U	Impeller tip velocity	[m/s]
V	Velocity	[m/s]
w	Relative velocity	[m/s]
W	Work	[J]
z	Blade number	[-]
α	Flow angle	[°]

β	Relative flow angle	[°]
β_b	Blade angle	[°]
γ	Specific heat ratio	[-]
δ	Winding angle	[°]
ϵ	Expansion ratio	[-]
ε	Specific energy	[J/kg]
ζ	Contraction ratio	[-]
η	Efficiency	[%]
Θ	Tank yield strength	[MPa]
λ	Exit swirl parameter	[-]
ν	Kinematic viscosity	
ξ	Combustion chamber characteristic length	[m]
ϖ	Residence time	[s]
ρ	Density	[kg/m^3]
σ	American slip factor	[-]
σ^*	European slip factor	[-]
σ_b	Cavitation coefficient	[-]
τ_{al}	Allowable shear stress	[MPa]
ϕ	Flow coefficient	[-]
ψ	Head coefficient	[-]
Ω	Power	[W]
ω	Angular velocity	[rad/s]

Subscripts

0	Stagnation conditions
1	Impeller inlet
2	Impeller exit
∞	No slip conditions
c	Combustion chamber
f	Fuel
h	Impeller hub, hydraulic conditions
i	Initial dry mass
imp	Impeller
inj	Injector
l	Losses
m	Mean
o	Oxidiser
p	Propellant
t	Blade tip

Superscripts

$*$	Throat condition

Abbreviations

ASReG	Aerospace Systems Research Group
CEA™	Chemical Equilibrium with Applications™
GM	Gravitational Model
INFF	Isentropic Nozzle Flow Functions
LEO	Low Earth Orbit
LOX	Liquid Oxygen
LVPC	Launch Vehicle Performance Calculator
NPSH	Net Positive Suction Head
NPSHR	Net Positive Suction Head Required
OA	Orbital Altitude
RP-1	Rocket Propellant-1
SAFFIRE	South African First Integrated Rocket Engine
SF	Safety factor
UKZN	University of KwaZulu-Natal

1. Introduction

1.1 The SAFFIRE programme

South Africa currently lacks the ability to deliver payloads into Low Earth Orbit (LEO). In response, and following an incremental approach, the University of KwaZulu-Natal's (UKZN) Aerospace Research Group (ASReG) is currently pursuing the design of an orbital rocket to provide an indigenous launch capacity for the country. The first step in such an endeavour, is the design of the propulsion system.

There are typically three categories of rocket engines, each defined by the state of the propellants, namely liquid, solid and hybrid (with hybrid rockets containing a liquid oxidiser and solid fuel). Liquid rockets tend to have higher specific impulses (*Isp*), than their counterparts, and have a greater degree of controllability, as the flowrate of the propellants can be regulated (Huzel and Huang, 1992). In addition, they are less politically controversial as compared to solid rockets that are frequently adopted in military programmes. These factors attributed to the decision that led to the inception of the South African First Integrated Rocket Engine (SAFFIRE). SAFFIRE is proposed to be a 25 kN thrust engine utilizing liquid oxygen and Rocket Propellant-1 (RP-1) as the oxidiser and fuel respectively. The power plant is designed to be modular in the sense that it can be clustered to form the booster stage of a vehicle. The small scale of the engine reduces the cost and complexity of testing the overall engine and the associated components.

Conventional liquid rocket engines make use of turbopump systems to pressurise the propellants prior to admission into the combustion chamber. There are three different system cycles, the gas generator, staged combustion and expander cycles. In all systems, the pumps are mechanically driven through a shaft (and sometimes a gearbox) by a turbine. The manner in which these turbines are powered is where the cycles differ. Figure 1-1 illustrates the process of each cycle.

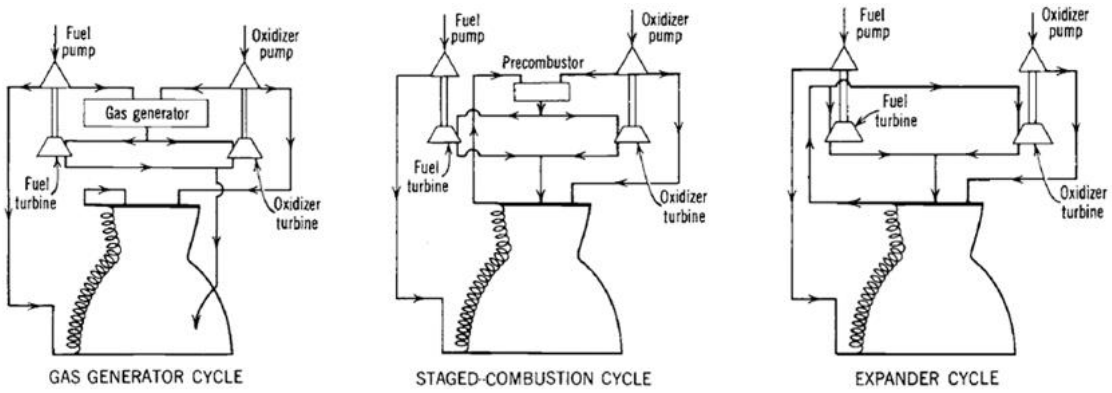

Figure 1-1: Three turbopump cycles used in liquid rocket engines (Sutton and Biblarz, 2001)

SAFFIRE intends to use an alternate approach, exploiting recent advances in battery technology. The turbopump is replaced with a high speed, electric motor driving a centrifugal pump. The electrically driven pump has been termed as an 'electropump' which has significant advantages over turbopumps. It mitigates the need for the turbine, gas generator/pre-combustor, drive shaft and any gearboxes; these components are large contributors to the engine's mass although the battery and motor masses may offset this weight reduction. The electrical system control is simplified and the complexity of the start-up sequence is reduced. Figure 1-2 is a schematic representation of the electropump system.

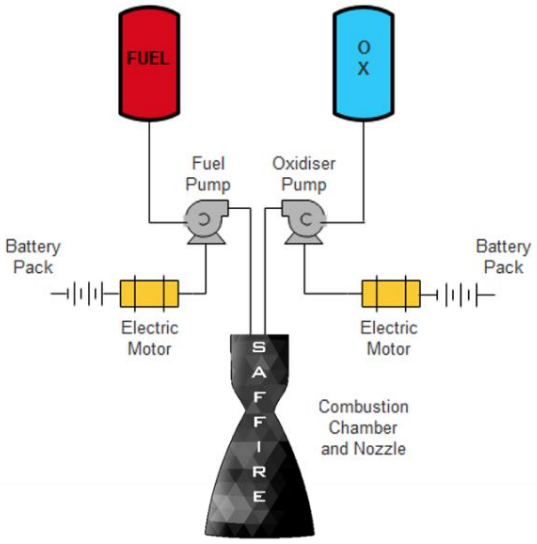

Figure 1-2: Schematic of the electropump system (Singh, 2017)

At the time of writing, only a single engine has ever implemented an electropump system, that being the Rutherford engine by New Zealand company Rocket Lab, which uses it to propel their reusable launch vehicle named Electron (Rocket Lab, 2017).

This work on the design of the fuel pump, together with the work of Nalendran Singh (Singh, 2017) on the oxidiser pump, form the foundation for SAFFIRE. The design began with the development of the electropump system, with specific focus on the hydrodynamic design of the fuel and oxidiser pumps (the latter being dealt with by Singh). As can be seen from Figure 1-3 the liquid rocket design process requires that a set of preliminary design decisions first be made before obtaining the hydrodynamic pump requirements. Part of the preliminary design decisions included the selection of the nozzle throat diameter and thrust output.

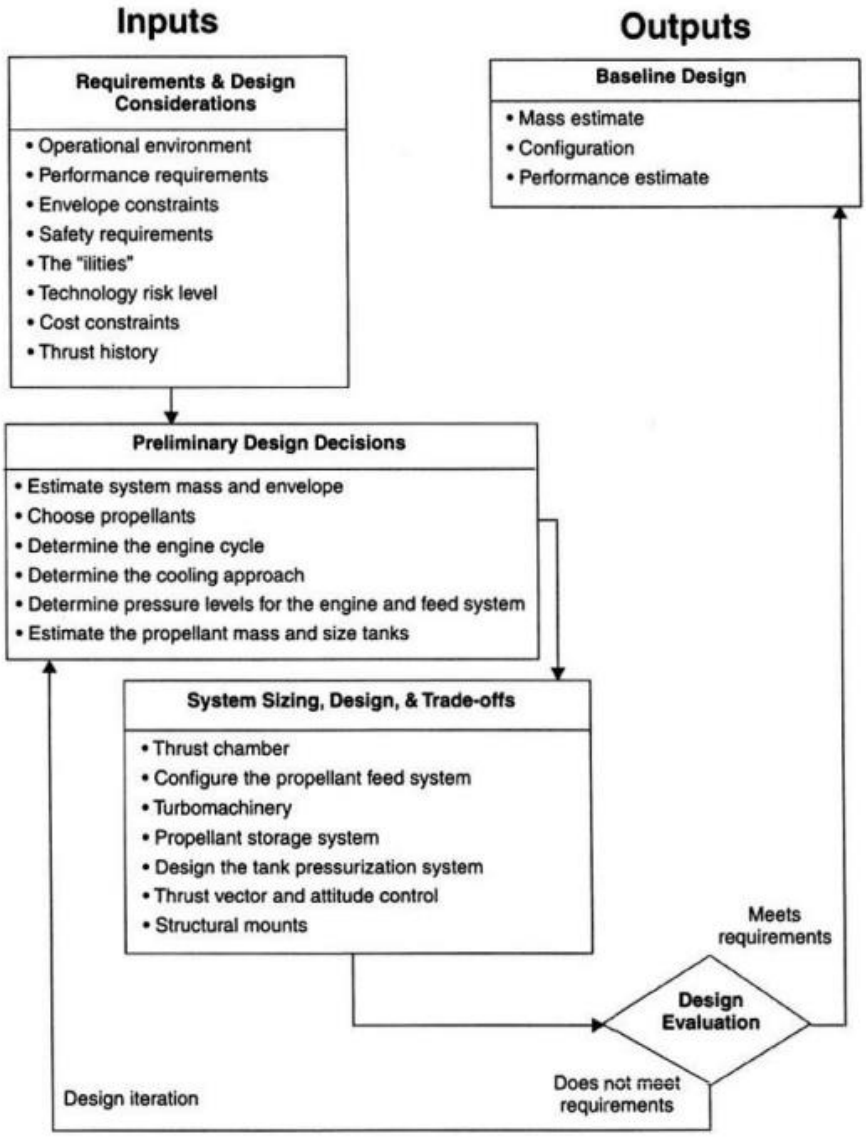

Figure 1-3: Liquid rocket design process flowchart (Humble et al., 1995)

In 2017, two additional students joined the SAFFIRE project. One was charged with the design of the engine injector while the second began the detailed design of the combustion chamber and nozzle.

The primary objectives of this work were to:

- Establish the engine and vehicle parameters, primarily the combustion chamber pressure, specific impulse, propellant mass flow rate, oxidiser to fuel ratio and engine burn time.
- Design a centrifugal pump that satisfies the hydrodynamic requirements of the engine, while minimizing weight and maximising efficiency.

1.2 Thesis outline

The present chapter introduces the SAFFIRE programme and design objectives. Chapter 2 discusses the engine specifications for SAFFIRE, as well as the methodology implemented to obtain the engine parameters. The chapter details the interdependent nature of the isentropic nozzle flow functions with the combustion analysis, and how the engine parameters are obtained. A hypothetical launch vehicle and mission are devised to determine an estimate of the engine's burn time.

Chapter 3 begins by outlining the hydrodynamic requirements of the pumps. The physics governing conventional centrifugal pump design are discussed, and a meanline impeller design algorithm is proposed thereafter. The fluid mechanic fundamentals are considered for the vaneless diffuser and scroll collection volute. The results of the conventional impeller design algorithm revealed a geometric problem that significantly influenced the hydrodynamic passage losses. The Barske pump was then investigated as an alternative design, due to potentially better efficiency at low specific speeds.

The generated designs were analysed in Chapter 4, using computational fluid dynamic (CFD) techniques. The Barske pump outperformed the conventional design, in terms of efficiency, by 9.3 %. The Barske design's observed flow field displayed a non-axisymmetric pressure distribution. The pressure imbalance resulted in a large nett radial thrust upon the impeller shaft which could lead to rotor instabilities. A hybrid design between a Barske impeller and scroll collection volute was thus investigated. The resultant pressure field, of the hybrid design, exhibited a greater degree of axisymmetry and a reduced radial thrust load.

Chapter 5 addresses cavitation in the impeller. Cavitation can be dealt with by the inclusion of an inducer or an increase in propellant tank pressure. An investigation was performed to determine how the vehicle mass changes with the changing tank pressure, and whether increasing the fuel tank pressure is a viable alternative to an inducer. Mass models for turbopump and electropump systems were developed. It was found that the suggested value drawn from literature of a 3 bar tank pressure would have been suitable had a turbopump system been used.

Chapter 6 summarises the final engine and pump parameters. It discusses the hydrodynamic conditions that led to the selection of the Barske impeller design and reasons for the variation in the optimal tank pressure between the turbopump and electropump systems. Recommendations are made thereafter with regards to further development of the fuel electropump for SAFFIRE.

2. Engine Specifications and Launch Vehicle Application

2.1 Introduction

Key performance requirements must be established before designing a rocket engine fuel pump. There are two main design criteria, namely the delivery pressure and mass flow rate of the pumping system. These design requirements are derived from the combustion chamber and nozzle design. The process for determining the vehicle's engine specifications is highly iterative. The minimum required combustion chamber pressure is determined using isentropic nozzle flow functions (INFF). The propellant's thermodynamic properties required for the INFF are obtained by performing a combustion analysis of the fuel and oxidiser, using NASA's Chemical Equilibrium with Applications™ (CEA) software. However, this analysis requires the combustion chamber pressure to be known. Thus, an iterative process exists between CEA™ and the INFF.

SAFFIRE is designed to be a modular propulsion system, used as either a single engine or as part of a cluster. A proposed mission is laid out for a hypothetical launch vehicle, utilising SAFFIRE, to demonstrate the potential application of the engine.

2.2 Methodology

In the design of a liquid rocket engine, the minimum required combustion chamber pressure is determined using the INFF, however the inputs required for the nozzle flow functions are obtained by performing a combustion analysis of the fuel and oxidiser at a prescribed operating combustion chamber pressure.

The methodical approach used to determine the engine characteristics requires the selection of two fixed parameters, namely the engine thrust output (*Ft*) and nozzle throat area (*A**). The INFF were used to calculate the minimum required chamber pressure for these fixed parameters. Four other input parameters are required for the INFF, namely specific impulse (*Isp*), specific heat ratio (γ), chamber stagnation temperature (T_{0c}) and the molecular weight of the gaseous product (*Mw*). These are also the outputs of the combustion analysis process from NASA's CEA™ software, which consequently requires the results of the INFF as an input. It is therefore necessary to provide estimated values, of the four variable input parameters to the INFF, for the first iteration of the closed loop process. The more accurate the estimated values

are, the fewer the iterations required. The iteration process converges when the outputs of the combustion analysis match the variable inputs of the INFF.

The operating time of the engine is also of importance for the design of the electrical drive system. Thus, the design and performance evaluation of a rudimentary, hypothetical launch vehicle was conducted. Estimates of the vehicle's dry masses were made to calculate the propellant mass for each stage and consequently the stage burn time. Figure 2-1 illustrates the methodology described above.

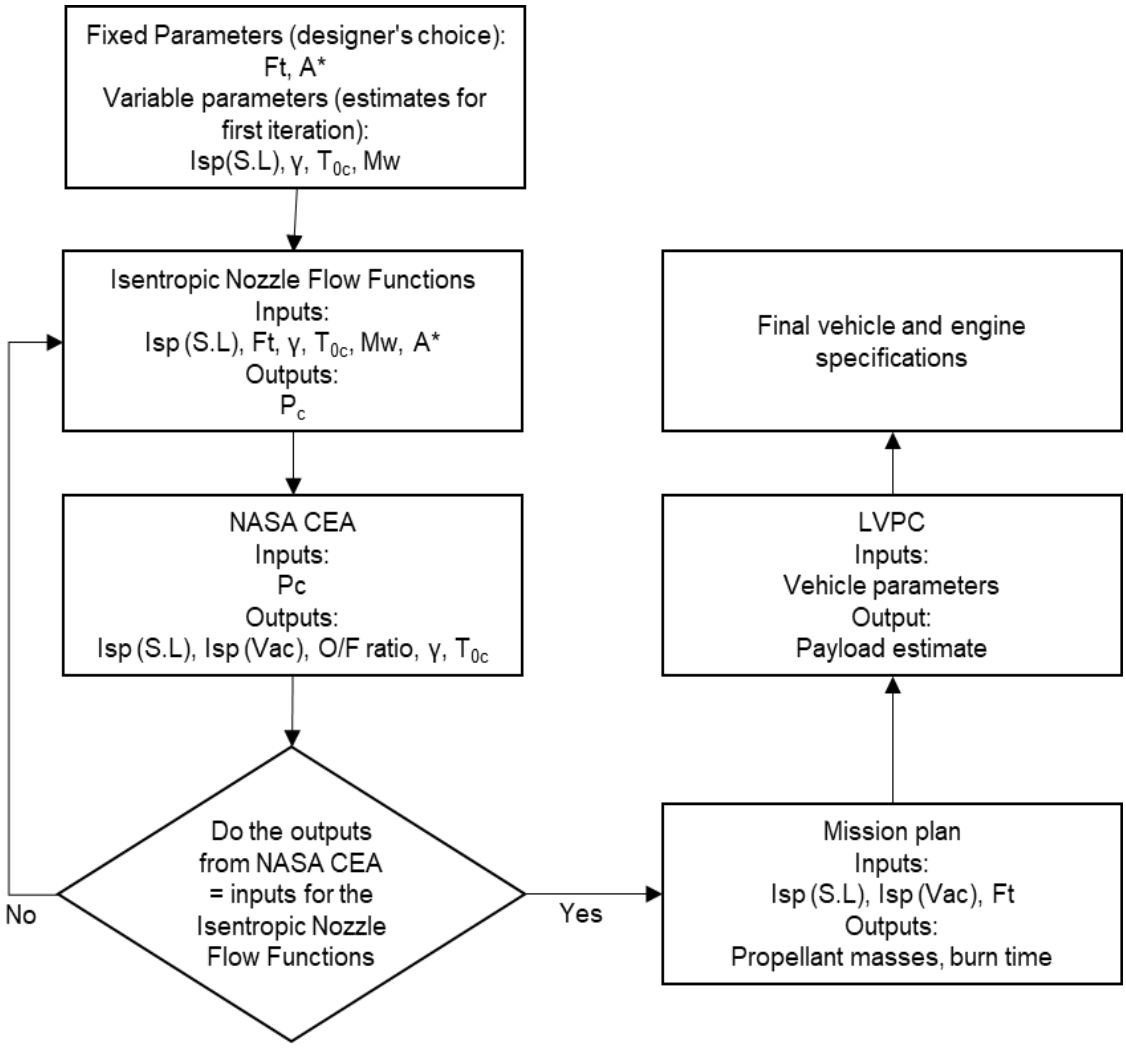

Figure 2-1: Flowchart depicting the methodology followed to obtain launch vehicle and engine specifications

2.3 Isentropic nozzle flow functions

Isentropic nozzle flow theory uses thermodynamic relationships between the inlet, throat and exit states of the nozzle under observation. In this work, the objective was to determine the minimum required chamber pressure at which the engine needs to operate to achieve the desired mass flow rate of propellant through the nozzle. The mass flow rate is calculated by setting the engine thrust (*Ft*) and the theoretical specific impulse (Isp) for the propellant combination of RP-1 and LOX. Using the definition of specific impulse in Equation 2.1, the total propellant mass flow rate ($\dot{m}_p$) can be calculated.

$$Isp = \frac{Ft}{\dot{m}_p\, g} \qquad [2.1]$$

In the above, g is the Earth's gravitational acceleration. The thermodynamic properties of the gaseous products, flowing through the nozzle, are assumed for the first iteration of the process. Thereafter the properties evaluated by the NASA CEA software are used for consequent iterations. The thermodynamic properties needed as inputs are the specific heat ratio (γ), combustion chamber stagnation temperature (T_{0c}), and the average molecular weight of the gaseous products (*Mw*).

The last input parameter for the INFF is the throat diameter (*D**), which sets the geometry of the combustion chamber via the nozzle contraction ratio (ϵ) and characteristic length (ξ). The characteristic length is defined in Equation 2.2 (Huzel and Huang, 1992) as the chamber volume over the nozzle throat area (*A**), where the chamber volume is a function of the propellant mass flow rate ($\dot{m}_p$) density of the combustion products (ρ_p) and the residence time needed for efficient combustion (ϖ).

$$\xi = \frac{\dot{m}_p \varpi}{\rho_p A^*} \qquad [2.2]$$

The characteristic length was set to 1.1 m, as recommended by Huzel and Huang (1992) for the propellant combination of LOX and RP-1. One of the assumptions made during the INFF calculation process was stagnation conditions within the combustion chamber. To ensure the validity of the assumption the contraction ratio was set to 4.1 as per Sutton and Biblarz (2001), who recommend a lower limit of 4. Thus, the chamber length (L_c) is a fixed value set by the

characteristic length and contraction ratio, as seen in Equation 2.3, while the cross-sectional chamber area (A_c) can be viewed as a function of the nozzle throat diameter (D^*), as given by Equation 2.4.

$$L_c = \frac{\xi A^*}{A^* \epsilon} = \frac{\xi}{\epsilon} \quad [2.3]$$

$$A_c = A^* \epsilon = (0.25)\, \pi {D^*}^2 \epsilon \quad [2.4]$$

Due to the chamber length being a fixed value, the aspect ratio (chamber diameter/chamber length) of the chamber depends solely on the nozzle throat diameter. Long and narrow chambers are more susceptible to non-isentropic pressure losses; conversely short chambers with a large cross-sectional area do not provide sufficient length for efficient mixing and combustion (Huzel and Huang, 1992). A throat diameter of 0.07 m was selected, which resulted in an aspect ratio of 0.53. The corresponding expansion ratio for an ideal, fully expanded flow is 6.73.

The minimum required chamber pressure may be calculated from the INFF thereafter. It is worth noting that the INFF assumes isentropic expansion of the flow through the nozzle, without the occurrence of flow separation or other irregular flow phenomena.

For the flow to accelerate from subsonic to supersonic speeds it must reach a speed of Mach 1 at the throat, at which point the nozzle becomes choked. The mass flow rate through the nozzle can be defined as the product of the local flow density (ρ^*), throat cross sectional area and velocity at the throat (c^*), as in Equation 2.5. Since the Mach number at the throat is 1, the velocity at the throat is simply the sonic velocity defined in Equation 2.6, where (T^*) is the local flow temperature at the throat. The local flow density at the throat can be redefined by the ideal gas law as a function of throat pressure, throat temperature and the specific gas constant (which is the universal gas constant divided by the molecular weight of the gaseous flow), seen in Equation 2.7.

$$\dot{m} = \rho^* A^* c^* \quad [2.5]$$

$$c^* = \sqrt{\gamma R T^*} \quad [2.6]$$

$$\rho^* = \frac{P^*}{RT^*} \quad [2.7]$$

By substituting Equations 2.6 and 2.7 into Equation 2.5, the mass flow rate becomes a function of two unknown parameters, namely the local throat pressure and temperature, Equation 2.8.

$$\dot{m} = \frac{P^* A^* \sqrt{\gamma R T^*}}{RT^*} \quad [2.8]$$

The local throat temperature (T^*) may be found from Equation 2.9, using a stagnation temperature (T_0) of 3716 °K and a Mach number of 1. The initial stagnation temperature is an assumption made by the author, based on literature. More accurate values of the stagnation temperature can be obtained after the first combustion analysis on NASA CEA.

$$\frac{T_0}{T^*} = 1 + \frac{\gamma - 1}{2} M^2 \quad [2.9]$$

The local static pressure at the throat can then be calculated from Equation 2.8, which then allows for the computation of the flow's stagnation pressure from Equation 2.10. The stagnation pressure can be assumed to be equal to the chamber pressure. This is due to the prior setting of the contraction ratio above 4, thus allowing for the assumption of stagnation conditions within the combustion chamber. The Mach number used in Equation 2.10 is 1, as throat conditions prevail.

$$\frac{P_0}{P^*} = \left(1 + \frac{\gamma - 1}{2} M^2\right)^{\frac{\gamma}{\gamma - 1}} \quad [2.10]$$

The calculated combustion chamber pressure is the minimum required pressure to accelerate the flow through the nozzle, from subsonic to supersonic speeds and to ensure choking of the flow at the throat. The calculated chamber pressure was 40.72 bar, however the final chamber pressure of 50 bar has a safety factor included to compensate for the non-isentropic losses which have not been considered.

2.4 Combustion analysis

The combustion process between the RP-1 and LOX is modelled using NASA's CEA™ software. The software performs the combustion analysis at a user prescribed pressure and oxidiser to fuel ratio (O/F ratio). The O/F ratio was listed as an output of the combustion analysis in Figure 2-1, this is because the combustion analysis is performed at varying O/F ratios to determine the optimal ratio for a peak sea-level specific impulse. Figure 2-2 shows the plotted results of the process, with the optimal O/F ratios being at 2.6 and 2.45 under vacuum and sea-level conditions respectively.

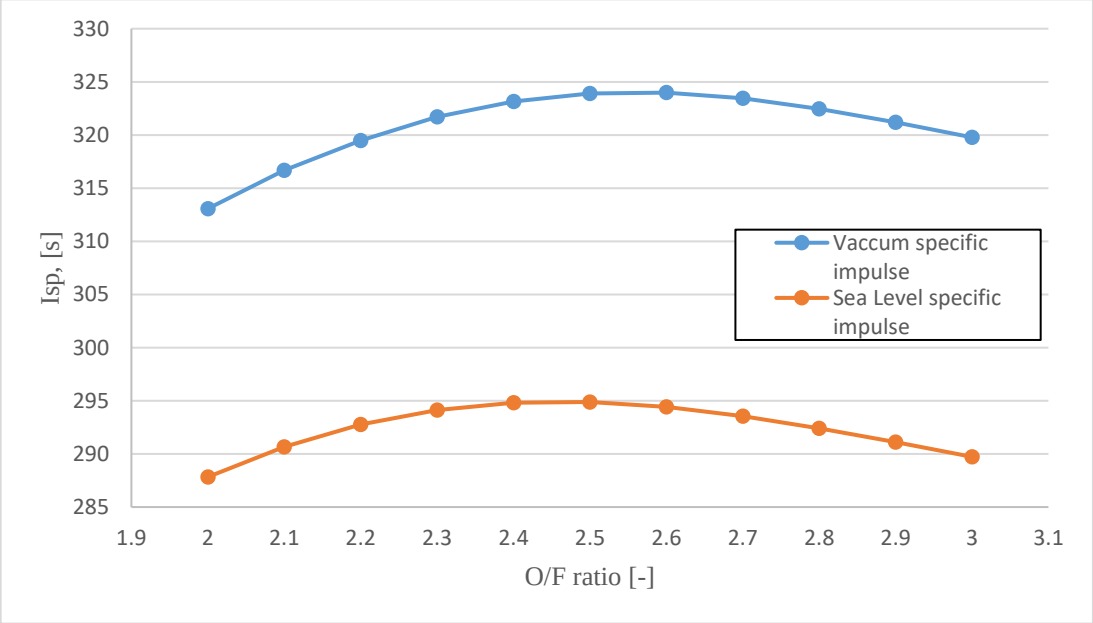

Figure 2-2: Specific Impulse versus O/F ratio for LOX-RP-1 at 50 bar chamber pressure

NASA CEA™ makes several assumptions in order to assess certain rocket parameters, such as the specific impulse. The assumptions made by the software include the following:

- One dimensional form of the energy, continuity and momentum equations
- Zero velocity at the combustion chamber inlet
- Complete combustion
- Adiabatic combustion
- Isentropic expansion in an idealized nozzle
- Homogenous mixing
- Ideal gas law
- Zero temperature and velocity lag between condensed and gaseous species

2.5 Hypothetical mission and launch vehicle

In order to ensure that the SAFFIRE engine is fit-for-purpose, it's capabilities must match the performance profile for the launch vehicle that it powers. To this end, a hypothetical mission was developed, from which estimated engine burn time could be obtained.

2.5.1 Proposed mission outline

The rapid advancement in the field of electronics has led to the development of increasingly smaller satellite technology. Nano-, micro- and small-satellites (1 kg – 500 kg) increasingly have the ability to perform identical tasks to those of their larger predecessors. This has reduced mission costs due to the reduced payload requirement of the launch vehicle as well the reduced surface area that lessens the effect of aerodynamic drag on the vehicle (Gallton, 2012). Whereas previous vehicle designs (using liquid engines) considered at UKZN were informed by the development of larger satellites, South Africa is unlikely to require launch capacity for satellites heavier than about 80 kg. Thus the previous design work by Smyth in 2014 (Smyth, 2014), must be revised to accommodate the future potential reliance on nano- and micro-satellites.

A CubeSat unit falls into the category of a pico-satellite (0.1 – 1 kg) with a volumetric standard of 10 cm cubed (Gashayija and Biermann, 2011). They can be configured as a multi-unit satellite capable of accommodating larger modules and instrumentation. Significant weight reduction together with increasingly powerful capabilities has led to cost reduction in their manufacture and a greater number of academic institutions and small-scale engineering firms are now participants in spacecraft development.

The SAFFIRE design programme is premised on the decision to pursue the development of a nanosat launch vehicle able to place several CubeSats in orbit with a single launch. The first stage engine configuration consists of an octagonal arrangement with a single central engine, as seen in Figure 2-3. The same engine configuration is used by SpaceX for the first stage of the Falcon 9 rocket (Figure 2-4) and is referred to as an Octaweb design. Smaller engines can be manufactured with more reliability, however clustering engines results in an increased number of systems, which increases the probability of a potential system malfunction (Huzel and Huang, 1992). There are two reasons for the selected cluster configuration. Firstly, the overall thrust requirement of the launch vehicle is distributed across the nine engines, consequently the mass flow rate required by each engine's electropump system is reduced by a factor of nine. This allows for the electropump systems to be tested without the need for an extensive and costly testing facility. Secondly, the smaller engine is considered more flexible as it can be

clustered in various configurations to meet different launch vehicle requirements for a variety of missions.

Figure 2-3: Proposed engine cluster configuration for SAFFIRE (Wunderlin, 2017)

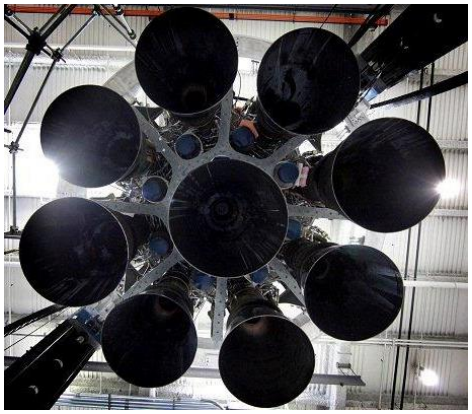

Figure 2-4: Falcon 9 Octaweb engine configuration (Space Exploration Technologies Corp., 2013)

Since the primary function of most cubesats is for earth observation, the required altitude for a SAFFIRE-powered vehicle in a sun-synchronous orbit is about 500 km, with a slightly retrograde (opposite to the Earth's rotation) orbital inclination of 97.4 degrees.

2.5.2 Mission planning and launch vehicle parameters

The proposed payload for the launch vehicle is 75 kg, which equates to approximately 15 cubesats including the associated deployment system. The vehicle inert stage masses are determined by the sum of the auxiliary equipment masses of each stage, which are made up from a plethora of components. It is difficult to calculate exact values for these masses, but

existing values from a similar launch vehicle (with similar mission objectives) can be used. In this case, the vehicle is Electron, powered by the Rutherford engine.

A specific amount of propellant is needed in order to get the prescribed payload to its destined orbit. The quantity of propellant for each stage of the launch vehicle can be calculated using the Tsiolkovsky rocket equation expressed as Equation 2.11. The only remaining unknown variable needed to solve for the propellant mass (m_p), is the required change in velocity (or commonly referred to as delta V) of the launch vehicle.

$$\Delta V = Isp.g.ln\frac{m_i}{m_i + m_p} \quad [2.11]$$

In the above, m_i is the initial dry mass of the vehicle. The delta V budget can loosely be seen as the blueprint of the mission. Each manoeuvre has an associated delta V cost. The typical ratio of the total delta V split between stages is 40/60 for the first and second stage respectively. This split is based upon design experience and was recommended by Schilling (2016). The total delta V requirement can be viewed as the sum of three other terms for a simplified direct ascent trajectory (Schilling, 2009).

$$\Delta V = V_{circ} + V_{rot} + V_{pen} \quad [2.12]$$

In the above, the circular orbit velocity term (V_{circ}) is the velocity needed for the vehicle to maintain a circular orbit at a prescribed orbital altitude (OA). This is described by Equation 2.13, where R_E is the Earth radius, m_E the mass of the Earth and G is Newton's gravitational constant.

$$V_{circ} = \sqrt{\frac{Gm_E}{R_E + OA}} \quad [2.13]$$

In Equation 2.12, the rotational velocity term (V_{rot}) represents the effect the Earth's rotation has on the vehicle's launch trajectory. It can be noted from the mission outline that the orbital inclination suggests a retrograde orbit, thus the contribution of the Earth's rotation is treated as a penalty. The value of the rotational velocity term can be computed using Newtonian physics and

geometry, needing only the latitude of the launch site and orbit inclination. In this study the proposed launch site would be the Denel Overberg Test Range (OTR) located at 34°33'17.9"S 20°15'01.6"E near the southern tip of Africa. The rotational velocity of the Earth at the launch site latitude is expressed in Equation 2.14.

$$V_{latitude} = R_E . \cos(34.36°) \frac{2\pi}{t_{day}} \quad [2.14]$$

where t_{day} is the time taken for a complete revolution of the Earth. The geometry used to relate the Earth's radius (R_E) to the radial distance from the axis of rotation to the latitude of the launch site (r_E), is depicted in Figure 2-5.

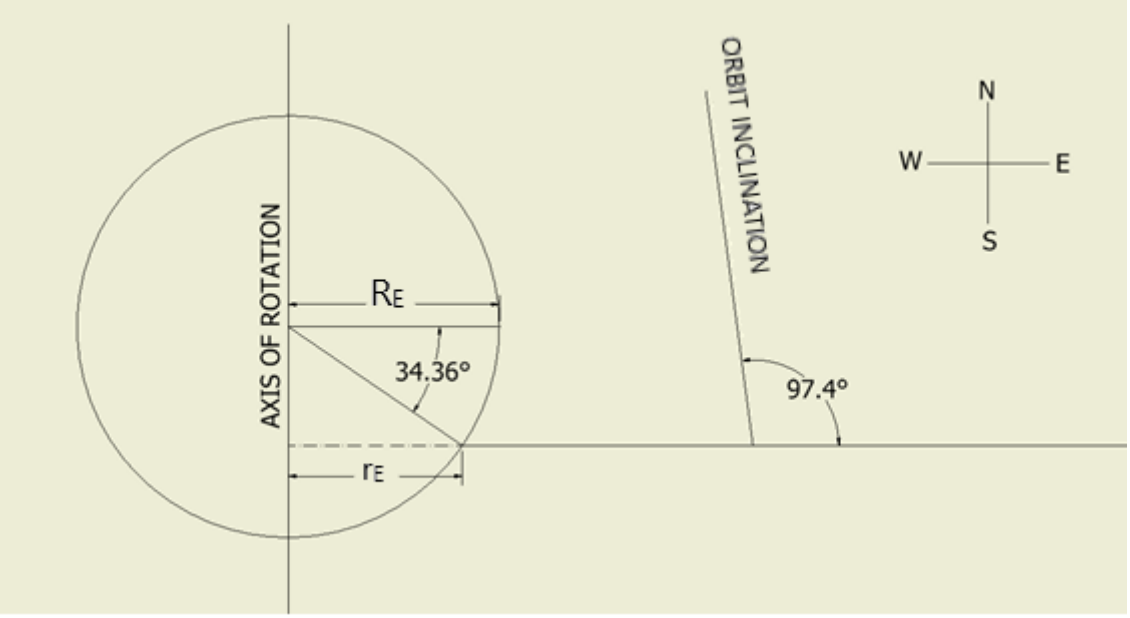

Figure 2-5: Geometry for calculating the Earth's rotational effect on delta V budget

The final contribution of the Earth's rotational velocity is calculated by taking the dot product of the Earth's velocity at the prescribed latitude along a unit vector in the direction of the vehicle's orbital inclination, resulting in Equation 2.15.

$$V_{rot} = \left| R_E . \cos(34.36°) \frac{2\pi}{\mathrm{T}} . \cos(97.4°) \right| \quad [2.15]$$

Lastly, the penalty term in Equation 2.12 represents the additional delta V required to overcome aerodynamic and gravitational drag. Townsend developed a penalty function to model these losses as a function of orbital altitude and ascent time, as reported by Schilling (2009) and given in Equation 2.16.

$$V_{pen} = 662.1 + (1.602)OA + (1.22 \times 10^{-3})(OA^2) + \cdots \quad [2.16]$$
$$\cdots (1.7871 - (9.687 \times 10^{-4})(OA))Ta$$

The ascent time of the vehicle is calculated by dividing the propellant mass for each stage by the mass flow rate of the exhaust propellant, (Equation 2.17).

$$Ta = \frac{m_p}{\dot{m}} \quad [2.17]$$

Together, Equations 2.11 to 2.17 form a closed system, as seen in Figure 2-6. The propellant mass needed to determine the ascent time is dependent upon a known total delta V. Therefore, the initial value of the aerodynamic and gravity drag penalty term is assumed in order to calculate an ascent time, thereafter Townsend's penalty function is used to calculate the penalty term. The discrepancy between the assumed and calculated value of the penalty term is evaluated; the assumed value is then altered with the objective of mitigating the discrepancy to within 1 m/s.

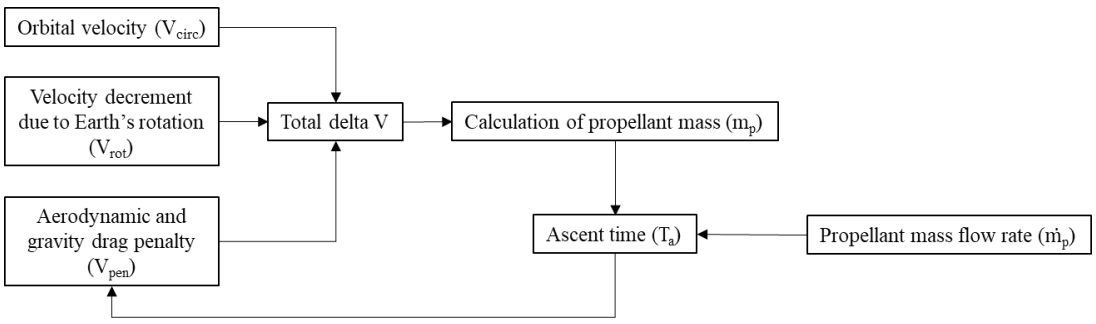

Figure 2-6: Determining the contribution of aerodynamic and gravity drag to the delta V budget

The final mission plan detailing the values of the delta V budget can be found in Table 2.1, while the vehicle specifications, per stage, are detailed in Table 2.2 and overall vehicle specifications in Table 2.3.

Table 2-1: Delta V budget

Orbital altitude for circular orbit *(OA)*	500 km
Radius of Earth *(R_E)*	6378 km
Earth model *(GM)*	3.9 x 10^{14} m^3/s^2
Circular orbital velocity *(V_{circ})*	7607 m/s
Earth rotational velocity *(V_{rot})*	49.5 m/s
Aerodynamic and gravity drag penalty *(V_{pen})*	2245 m/s
Total delta V for orbit insertion	9901.4 m/s

Table 2-2: Launch vehicle parameters per stage

	1st stage	**2nd stage**
Dry mass	950 kg	250 kg
Final mass *(m_f)*	3380.9 kg	375 kg
Propellant mass *(m_p)*	9905.2 kg	2055.9 kg
Specific Impulse *(Isp)*	295 s	324 s
Mass ratio *(final/initial)*	0.25	0.15
Delta V per stage	3960.6 m/s	5940.8 m/s
Propellant mass fraction *(m_p/m_i)*	0.75	0.85

Table 2-3: Overall launch vehicle parameters

Take-off thrust to weight ratio	1.7
Payload	75 kg
Fairing mass	50 kg
Jettison time	127.4 s
Total ascent time	365.4 s

The Silverbird™ LVPC is used to determine a payload estimate as a function of orbital altitude for the designed vehicle. The vehicle parameters are entered into the LVPC along with the launch site details. The results of the payload estimate for varying orbital altitudes are depicted in Figure 2-7.

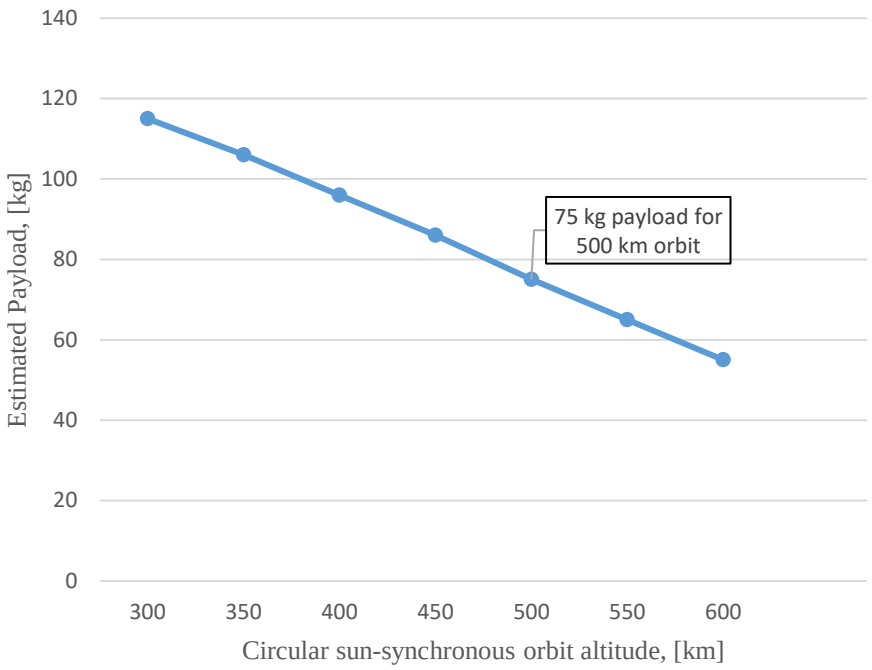

Figure 2-7: Payload estimate as a function of orbital altitude

2.6 Conclusion

The final engine specifications provide important design criteria for the electropump system. The combustion chamber pressure provides the basis for calculating required pump delivery pressure. The specific impulse and oxidiser to fuel ratio, obtained from the combustion analysis, provides the information necessary to determine the mass flow rates of the fuel and oxidiser pump respectively. The mission plan and launch vehicle design primarily gave credence to the design of SAFFIRE, however the burn time of the vehicle provides necessary information for the design of the electrical drive system of the electropump. The first stage burn time is calculated to be 116s. The final engine specifications for SAFFIRE can be found in Table 2-4.

Table 2-4: Final engine specifications for SAFFIRE

Parameters for a single engine	**Sea level conditions**	**Vacuum conditions**
Thrust	25 kN	27.46 kN
Min chamber pressure required	40.72 bar	40.72 bar
Recommended chamber pressure	50 bar	50 bar
O/F ratio	2.45	2.6
Mass flow rate of propellants	8.64 kg/s	8.64 kg/s
Mass flow rate of oxidiser	6.13 kg/s	6.24 kg/s
Mass flow rate of RP-1	2.50 kg/s	2.40 kg/s
Isp	295 s	324 s

3. Hydrodynamic Pump Design

3.1 Introduction

The hydrodynamic design of the electropump involves three primary components, namely the impeller, diffuser and volute. The type of pumping system selected is based upon the pump requirements. Rocket engine turbopumps are typically of the radial type because the requirements of the engine usually match the operating range in which radial pumps have higher efficiencies over other pump types. This chapter details the preliminary design of each core pump component.

There are two primary design objectives for turbopumps; first to minimize the pump size to reduce overall engine weight and thereby maximize the engine efficiency and secondly, to maximize the efficiency of the pump itself, thus reducing the amount of fuel carried by the vehicle to drive the pump. In the case of the electropump, optimized efficiency reduces the number of batteries needed. The first of the two objectives can be addressed during the single-zone meanline design process. Maximising the impeller efficiency is a difficult task, and not feasible using meanline methods; this is because, in order to measure efficiency, the flow field through the impeller must be known. Analytical methods have failed to provide adequate meanline models that accurately predict the flow fields through an impeller passage. For this reason, many turbomachinery text books place emphasis on the use of experience for a preliminary design. Experience will usually guide the designer as to what fundamental geometric parameters would yield an acceptable flow field and hence an efficient design. An iterative process begins whereby the flow field for a selected geometry is analysed using CFD or experimental methods, thereafter the design is refined and the process continues until an acceptable level of efficiency is obtained. Work is being done on inverse impeller design methods using potential flow field functions with integrated CFD methods (Westra, 2008), however this would still require large computing clusters, and is yet to become a rapid inverse design solution.

3.2 Pump system requirements

Chapter 2 dealt with the development of the engine specifications, which provides the basis for deriving the pumping system requirements. The required mass flow rate through the fuel pump is found by using the total propellant mass flow rate through the nozzle and the oxidiser to fuel ratio. The fuel mass flowrate is 2.5 kg/s, however, historically the fuel in liquid rocket engines

has been used for cooling the nozzle and combustion chamber, thus an additional 10% of fuel may be required for film cooling, bringing the design mass flow rate to 2.75 kg/s

The nominal combustion chamber design pressure ($P_{combustion}$) is 50 bar. The delivery pressure of the pump needs to be substantially higher to accommodate for hydraulic losses in the feed system and the requisite pressure drop across the injector. The total pump delivery pressure can be estimated by creating a mock feed system model (Table 3-1) and calculating the associated losses using Equation 3.1 derived using Bernoulli's equation. The recommended pressure drop across the injector is said to be 20% of the combustion chamber pressure (Huzel and Huang, 1992). The pressure drop is designed to isolate the feed system upstream of the injector from any pressure oscillations within the chamber.

Table 3-1: Mock feed system parameters

Effective pipe length *(L_e)*	5 m
No. of bends	2
Friction factor *(f)*	0.042
Injector loss *(P_{inj})*	10 bar
Internal pipe diameter *(d)*	0.03 m
Kerosene density *(ρ)*	819 kg/m^2
Kinematic viscosity of kerosene	1.814 x 10^{-6} m^2/s

$$P_{pump} = \rho g \left(H_{fr} + \sum H_l \right) + P_{inj} + P_{combustion} \quad [3.1]$$

The head loss due to pipe friction and the minor losses due bends and fittings are calculated as per Equation 3.2 and Equation 3.3 respectively.

$$H_{fr} = f \frac{L_e}{d} \left(\frac{{V_f}^2}{2g}\right) \quad [3.2]$$

$$H_l = K_x \frac{{V_f}^2}{2g} \quad [3.3]$$

where (K_x) is a unique loss coefficient for each fitting.

The friction factor is determined by finding the Reynolds number of the flow through the piping system and using the corresponding value to find the friction factor on a Moody diagram, (Figure A.1, Appendix A).

The total delivery pressure required by the pump (H_{req}) is 61.7 bar.

3.3 Conventional meanline impeller design

The baseline impeller design involves treating the flow through the passages in a one-dimensional fashion. The single zone model deals with control surfaces at the impeller inlet and exit. The modelled flow is also assumed to behave in an isentropic manner, neglecting the formation of secondary flows.

3.3.1 Impeller inlet

The design of the impeller inlet involves the relative flow interaction between the pump inlet and the leading edge of the impeller blades. Figure 3-1 shows a generic velocity triangle that can be used for hub, tip and mean flow calculations. The absolute inlet flow velocity (assumed to be purely axial due to the absence of inlet guide vanes) is based upon the impeller hub and tip radii as in Equation 3.4 and represented as (C_1) in Figure 3.1.

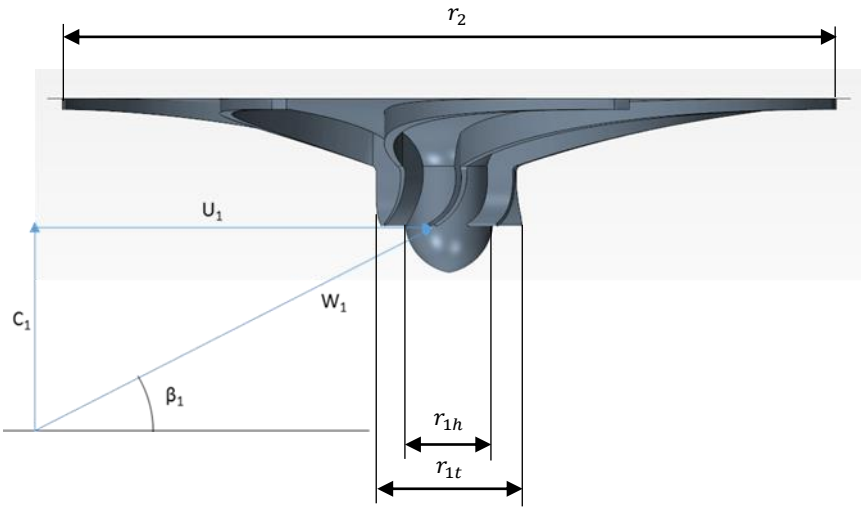

Figure 3-1: Generic impeller inlet velocity diagram

$$C_1 = C_{m1} = \frac{\dot{m}}{\rho_f \pi ({r_{1t}}^2 - {r_{1h}}^2)} \quad [3.4]$$

There is assumed to be no swirl at inlet, thus $C_\theta = 0$.

The inlet hub radius (r_{1h}) is set as the minimum required shaft radius to prevent shaft failure, multiplied by a safety factor (*SF*) of 1.8, as seen in Equation 3.5 (Gülich, 2007). The material chosen for the shaft is 316 stainless steel which has an allowable shear stress (τ_{al}) of 118.9 MPa.

$$r_{1h} = \frac{1}{2}\left(\frac{480\Omega_{imp}}{\pi^2 N \tau_{al}}\right)^{\frac{1}{3}} \times SF \quad [3.5]$$

In the above, *N* is the rotational speed of the impeller in revolutions per minute. For the above calculation to be performed, the hydraulic power consumed by the impeller (Ω_{imp}) must be determined via Equation 3.6, with an empirical correlation defining an estimated hydraulic stage efficiency (η_h) in Equation 3.7 (Gülich, 2007).

$$\Omega_{imp} = \frac{\left(\rho_f g Q H_{req}\right)^{\frac{1}{3}}}{\eta_h} \quad [3.6]$$

$$\eta_h = 1 - 0.055\left(\frac{1}{Q}\right)^m - 0.2\left(0.26 - log\left(\frac{n_q}{25}\right)\right)^2 \left(\frac{1}{Q}\right)^{0.1} \quad [3.7]$$

where $m = 0.08a\left(\frac{1}{Q}\right)^{0.15}\left(\frac{45}{n_q}\right)^{0.06}$ and $a = 1$ as the volumetric flowrate is less than 1 m^3/s.

The specific speed (n_q) used in Equation 3.6 is defined as follows in Equation 3.8.

$$n_q = \frac{N Q^{0.5}}{{H_{req}}^{0.75}} \quad [3.8]$$

By combining Equations 3.5 through to 3.8, the hub radius becomes a function of the impeller rotary speed (N), system flow rate (Q), system head rise (H_{req}) and allowable shear stress (τ_{al}). The system flow rate and head rise can be viewed as fixed parameters set by the engine specifications. Therefore, the hub radius can be viewed as a function of only impeller speed, mathematically expressed as $r_{1h} = f(N)$. Before defining the inlet tip radius, the Net Positive Suction Head Required (NPSHR) by the impeller must be determined. The NPSHR defines the stagnation pressure at the impeller inlet that would result in cavitation inception. Cavitation is the process whereby the local static pressure drops below the working fluid's vapour pressure due to local flow acceleration. This results in the formation of vapour bubbles on the blade surface; the bubbles then may later implode causing material damage to the impeller which is an undesirable consequence.

The cavitation inception point is represented by Equation 3.9. where the static pressure at the tip (P_{1t}) is reduced to the vapour pressure (P_v) due to the local flow acceleration. The impeller tip is dealt with as it has the highest circumferential velocity along the blade leading edge.

$$P_v = P_{1t} - \sigma_b \left(\frac{1}{2}\rho {w_{1t}}^2\right) \tag{3.9}$$

The blade cavitation coefficient (σ_b) represents the fraction of the relative inlet dynamic pressure involved in local flow acceleration (where w_{1t} is the relative flow velocity). The blade cavitation coefficient is unique to each pump, and is usually found through experimentation, however Japikse et al. (2006) recommend a value of 0.1 for rocket turbopumps. The static pressure term (P_{1t}) can be rewritten in terms of the stagnation and dynamic pressure components as in Equation 3.10. The NPSHR can be written explicitly (Equation 3.11) by rearranging Equation 3.10.

$$P_v = P0_1 - \left(\frac{1}{2}\rho {C_1}^2\right) - \sigma_b \left(\frac{1}{2}\rho {w_{1t}}^2\right) \tag{3.10}$$

$$NPSHR = \frac{P0_1 - P_v}{\rho g} = \frac{\left(\frac{1}{2}{C_1}^2\right) + \sigma_b \left(\frac{1}{2}{w_{1t}}^2\right)}{g} = \frac{\frac{1}{2}{C_1}^2(1+\sigma_b) + \frac{1}{2}\left(\frac{r_{1t}\pi N}{30}\right)^2}{g} \tag{3.11}$$

The NPSHR is thus a function of the absolute inlet velocity (C_1), impeller speed (N) and the inlet tip radius of the impeller (r_{1t}). The inlet tip radius is calculated from Equation 3.12, which optimizes the inlet tip radius for minimum inlet kinetic energy and consequently improved overall efficiency (Japikse et al., 2006).

$$r_{1t} = \sqrt{{r_{1h}}^2 + 2^{\frac{1}{3}}\left[\frac{30Q}{\pi^2 N}\right]^{\frac{2}{3}}} \qquad [3.12]$$

The inlet tip radius can now be viewed as a function of the hub radius and impeller speed, but $r_{1t} = f(r_{1h}, N)$ and $r_{1h} = f(N)$ thus $r_{1t} = f(N)$. Now that the inlet hub and tip radii are both defined as functions of impeller speed, the absolute inlet velocity (Equation 3.4) can also be also be explicitly defined in terms of speed, $C_1 = f(N)$. Consequently, the NPHSR can also be viewed as a function of impeller speed, $NPSHR = f(C_1, r_{1t}, N) = f(N)$.

The only remaining parameters for the inlet design are the inlet blade angles. These are calculated from the velocity triangle in Figure 3.1 using basic trigonometry. The inlet blade angle varies from hub to tip as seen in Equation 3.13.

$$\beta_1 = \tan^{-1}\frac{30C_1}{r_x \pi N} \qquad [3.13]$$

where, $r_x = r_{1h}, r_{1t}, r_{1m} = f(N)$. Therefore, all inlet parameters are a function of the impeller speed, $C_1, r_{1h}, r_{1t}, NPSHR, \beta_1 = f(N)$.

3.3.2 Impeller exit

The fluid flow at the impeller exit can be described by the velocity vector diagram in Figure 3-2. The vector diagram relates the relative velocity leaving the impeller passage to an absolute frame of reference. The effect of slip is also included in the vector diagram and is crucial in the development of a meanline impeller design. The term ‘slip’ is used to describe the deviation of the relative flow exiting the impeller passage; this is due to the uneven pressure distribution across the width of the impeller passage in the blade-to-blade direction.

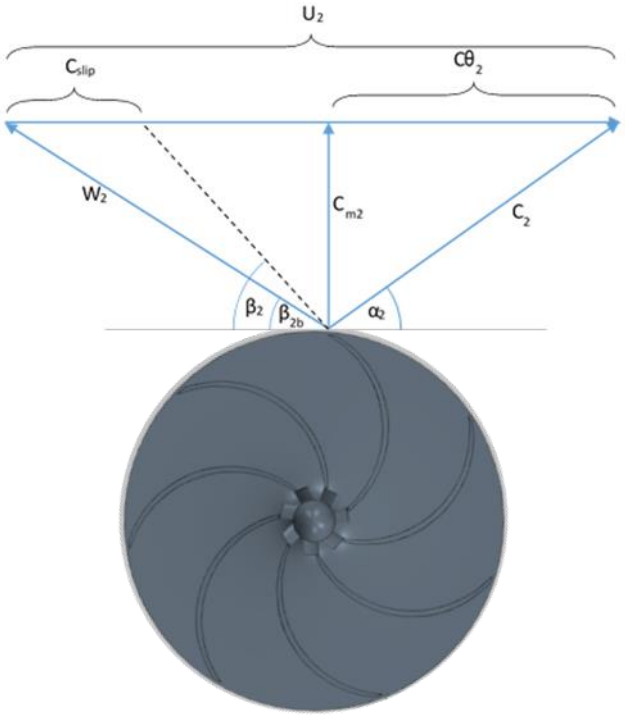

Figure 3-2: Impeller exit velocity vector diagram

One of the most fundamental equations in the field of turbomachinery is the Euler turbomachinery equation represented in Equation 3.14, which defines the hydraulic work done by a rotor. It forms part of a hydraulic energy balance (defined by Equation 3.15) with a control volume taken around the impeller. For impellers designed to operate at the best efficiency point, the backflow loss can be approximated as zero (Japikse et al., 2006). Equation 3.16 represents the nett specific hydraulic work done by the pump and Equation 3.17 determines the specific energy loss due to disk friction.

$$W_{imp} = \Delta U C_\theta = U_2 C_{\theta 2} - U_1 C_{\theta 1} \quad [3.14]$$

$$W_x = W_{imp} + W_{disk\ friction} + W_{backflow} \quad [3.15]$$

$$W_x = \frac{g \Delta H_{req}}{\eta_h} \quad [3.16]$$

$$W_{disk\ friction} = \frac{-\Omega_{disk\ friction}}{\dot{m}} \quad [3.17]$$

The estimated hydraulic efficiency term was calculated using Equation 3.7. The power consumed by disk friction ($\Omega_{disk\ friction}$) is defined by Equation 3.18 (Nemdili, 2004):

$$\Omega_{disk\ friction} = (CM)\rho\omega^3 {r_2}^5 \quad [3.18]$$

where *CM* is the torque coefficient and is empirically determined using the correlation given in Equation 3.19, developed by Daily and Nece (1960).

$$CM = \frac{0.0102\left(\frac{s}{r_2}\right)^{0.1}}{Re^{0.2}} \quad [3.19]$$

where 's' denotes the axial clearance between the rotor and shroud. The Reynolds number is defined in Equation 3.20.

$$Re = \frac{\omega r_2^2}{\nu} \quad [3.20]$$

In the above, ν is the kinematic viscosity of the fluid and ω is the angular velocity of the impeller. The conventional slip factor follows the American definition in Equation 3.21, where U_2 is the blade tip velocity of the impeller (Japikse et al., 2006).

$$C_{slip} = U_2(1 - \sigma) \quad [3.21]$$

A second definition of the slip factor ($\sigma*$), known as the European definition, is defined in Equation 3.22, where $C_{\theta 2\infty}$ represents the absolute tangential velocity under no slip conditions.

$$\sigma* = \frac{C_{\theta 2}}{C_{\theta 2\infty}} \quad [3.22]$$

The two slip factor definitions have the relationship shown in Equation 3.23 (Japikse et al., 2006).

$$1 - \sigma = \frac{C_{\theta 2}}{U_2}\left(\frac{1}{\sigma *} - 1\right) \quad [3.23]$$

Thus, rewriting Equation 3.21 in terms of the European slip factor results in Equation 3.24.

$$C_{slip} = C_{\theta 2}\left(\frac{1}{\sigma *} - 1\right) \quad [3.24]$$

An empirical correlation was developed by Pfleiderer in 1961 to determine an estimated slip factor (Equation 3.25) based on the interaction between the method of diffusion, blade number (z) and blade exit angle (β_{2b}) (Japikse et al., 2006):

$$\frac{1}{\sigma *} = 1 + \frac{a}{z}\left(1 + \frac{3\beta_{2b}}{\pi}\right)\frac{2}{1 - \frac{r_1^2}{r_2^2}} \quad [3.25]$$

where $a = 0.85$ for a vaneless diffuser.

The number of blades required by an impeller varies as per the flow characteristics through the impeller passage. A greater number of blades reduces the blade-to-blade loading and results in a more uniform flow field, however this leads to increased blockage due to a greater number of boundary layers being formed. Too few blades result in the propagation of cross passage flow and non-uniform exit velocity profiles. The recommended exit blade number for the preliminary design is 7 (Gülich, 2007), and is used as a fixed parameter for the remainder of the conventional meanline design process.

Equation 3.26 provides a relationship between the previously defined absolute tangential velocity, slip velocity and impeller tip velocity. The relationship is derived from the addition of the appropriate vectors found in the impeller exit velocity triangle in Figure 3-2.

$$U_2 = C_{\theta 2} + C_{slip} + C_{m2}\tan\left(\frac{\pi}{2} - \beta_{2b}\right) \quad [3.26]$$

The meridional velocity at exit (C_{m2}) is defined in Equation 3.27.

$$C_{m2} = \frac{Q}{2\pi r_2 b_2} \qquad [3.27]$$

3.3.3 Impeller design algorithm

Conventional direct design methods would assume an impeller speed and work through the governing inlet equations in a linear manner. The difficulty with this method is the arbitrary selection of the impeller speed. Part of the preliminary design objectives was to maximise the impeller speed, which reduces the overall size and weight of the pump. The hydrodynamic requirements place the potential operating range of the pump in the shaded area on Figure 3-3. Increasing the operating speed, with fixed head rise and flow rate, results in increasing specific speed and consequently improved efficiency. At high speeds, the possibility of cavitation exists and therefore a limitation on the net positive suction head (NPSH), at which the impeller operates, is imposed to find the maximum speed at which the impeller can operate without cavitation. The recommended operating NPSH is taken to be 20% of the NPSHA (Huzel and Huang, 1992). The NPSHA is defined as the pressure head difference between the total stagnation pressure at the pump inlet and the vapour pressure of the working fluid.

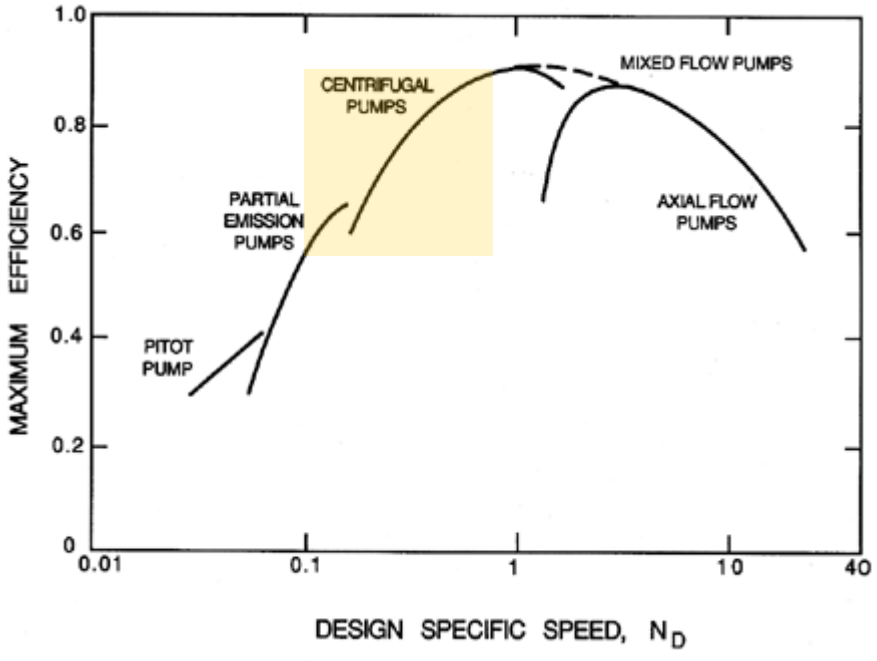

Figure 3-3: Pump efficiency vs. dimensionless specific speed (Balje, 1981)

The impeller speed is selected through an iterative process by varying the impeller speed until an NPSH equal to 20% of the NPSHA has been achieved. An initial guess of impeller speed is required for the first iteration. The inlet geometry is then calculated as per section 3.2.1, as all the inlet parameters were shown to be a function of impeller speed.

$$C_1, r_{1h}, r_{1t}, NPSHR, \beta_1 = f(N)$$

The desired NPSH is defined by Equation 3.28.

$$NPSH = 0.2 * NPSHA = NPSHA - NPSHR \quad [3.28]$$

$$\therefore NPSHR = 0.8 * NPSHA$$

The error between the NPSHR computed from Equation 3.11 and the desired NPSHR is calculated. The magnitude and sign of the error dictates how the impeller speed must be adjusted to ensure convergence. Figure 3-4 describes the iterative process involving the impeller inlet design equations and speed increment selection based upon the observed error. The larger the error, the larger the incremental step size for the impeller speed adjustment. This reduces the computational time of the algorithm. To ensure that the error does not continuously diverge, the algorithm compares errors between a predetermined number of iterations and changes the sign of the increment if necessary. The MATLAB™ script written by the author and used for the impeller inlet design can be found in Appendix B.

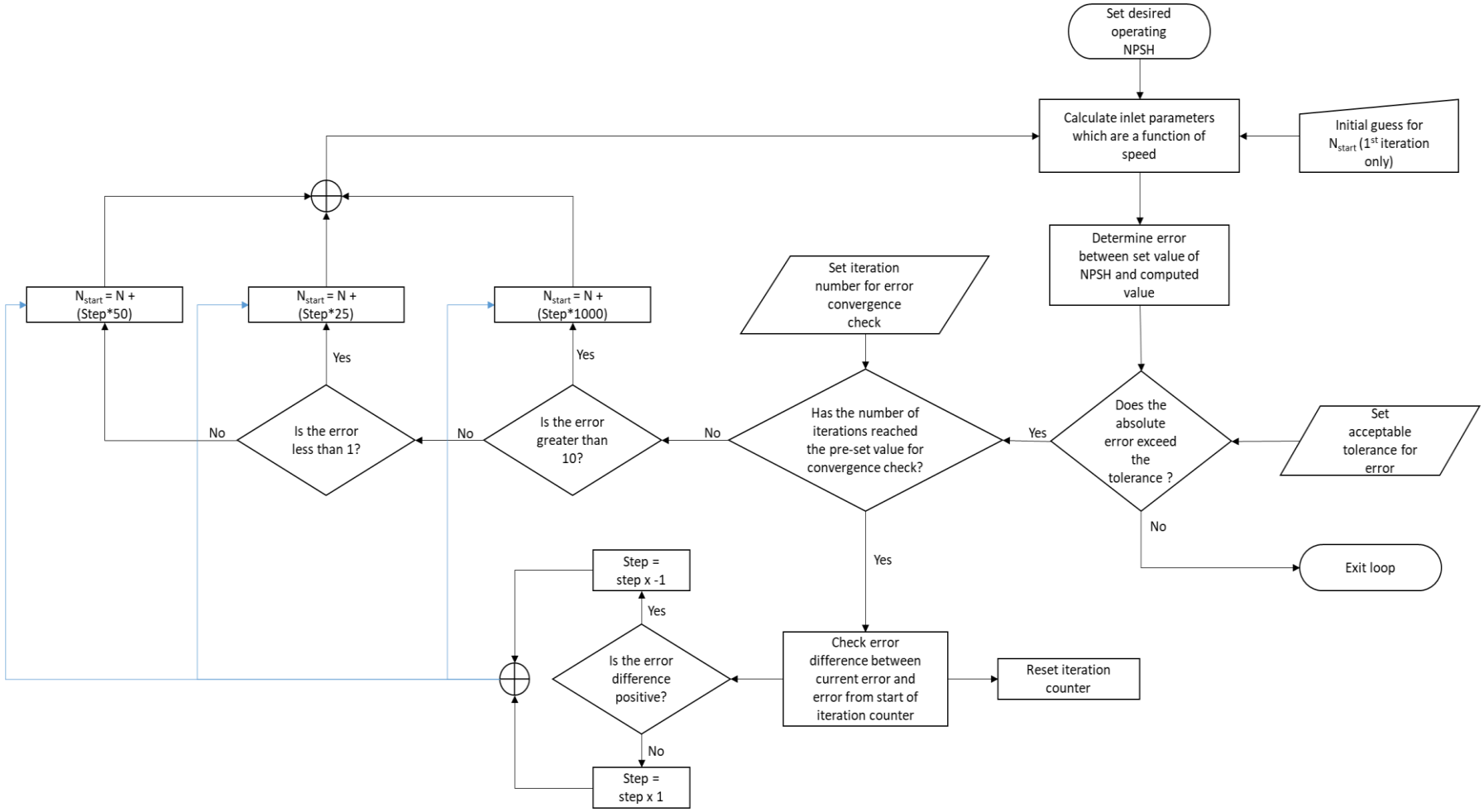

Figure 3-4: Inlet design process for impeller speed

The impeller exit radius (r_2) is implicitly solved as a function of blade exit angle and the exit swirl parameter. The exit swirl parameter is defined as the ratio between the tangential exit velocity and meridional exit velocity. It represents the impeller's propensity for recirculation at the impeller exit, with higher values indicating a greater probability of recirculation. The dependent variable (r_2) is constrained by two equations, the specific energy equation (represented by Equation 3.14) and the vector relationship that arises from the exit velocity triangle defined by Equation 3.26. A single governing equation is created by combining Equations 3.14 to 3.20 to form Equation 3.29:

$$C_{\theta 2} = A{r_2}^{-1} + B{r_2}^{-1} \quad [3.29]$$

where:

$$A = \frac{g\Delta H_{required}}{\omega \eta_h}$$

$$B = \frac{0.0102(s)^{0.1}\rho\omega}{\dot{m}}$$

Equation 3.24 and the slip definition are substituted into Equation 3.26, which results in Equation 3.30, derived by the author below:

$$C{r_2}^{4.9} + D{r_2}^{4} + E{r_2}^{2.9} + F{r_2}^{2} + G = 0 \quad [3.30]$$

In the above:

$$C = B\left(\left(1 + \frac{1}{\lambda}\tan(90° - \beta_{2b})\right) + \left(\frac{2a}{z}\left(1 + \frac{\beta_{2b}}{60}\right)\right)\right)$$

$$D = -\omega$$

$$E = -\left(B\left(1 + \frac{1}{\lambda}\tan(90° - \beta_{2b})\right)\right){r_1}^{2}$$

$$F = {r_1}^2\omega + A\left(\left(1+\frac{1}{\lambda}\tan(90° - \beta_{2b})\right)+\left(\frac{2a}{z}\left(1+\frac{\beta_{2b}}{60}\right)\right)\right)$$

$$G = \left(-\left(A\left(1+\frac{1}{\lambda}\tan(90° - \beta_{2b})\right)\right)r_{1m}\right)^2$$

The exit radius is then implicitly solved from Equation 3.30. The coefficients present in the above equations are referred to as pseudo-constants, as the independent variables (exit swirl parameter (λ) and blade exit angle (β_{2b})) are increasingly incremented for each iteration of the algorithm.

There is an embedded exception stemming from the Pfleiderer slip factor. A check is implemented to determine if the ratio of the mean inlet radius (r_{1m}) to exit radius (r_2) is greater or equal to 0.5. If the check returns a false result the ratio of inlet to exit radii is set to 0.5 (Japikse et al., 2006). The governing equation presented as Equation 3.30 is now altered to accommodate the change in the Pfleiderer correlation, and it takes the form of Equation 3.31.

$$K{r_2}^{2.9} + D{r_2}^2 + J = 0 \qquad [3.31]$$

where:

$$H = \frac{a}{z}\left(1+\frac{\beta_{2b}}{60}\right)\frac{2}{1-0.5^2}$$

$$I = 1 + H + \frac{1}{\lambda}\tan(90° - \beta_{2b})$$

$$J = AI$$

$$K = BI$$

Once the exit radius has been solved for, the other impeller parameters may be calculated using the relationships presented in subsections 3.2.1 and 3.2.2. Figure 3-5 illustrates the impeller exit radius plotted as a function of the blade exit angle and the exit swirl parameter. The exit swirl parameter represents the ratio between the tangential and meridional velocities at the impeller exit. Increasing the exit swirl parameter results in more diffusion but decreased stability; the inverse holds true for decreasing the parameter. Figure 3-6 depicts an experienced based guide

of recommended exit swirl parameters as a function of specific speed. The specific speed of the pump design is 472 (metric definition) and is represented by the vertical, orange line on Figure 3-6. Thus, the design range for the exit swirl parameter is between 6.5 and 16.

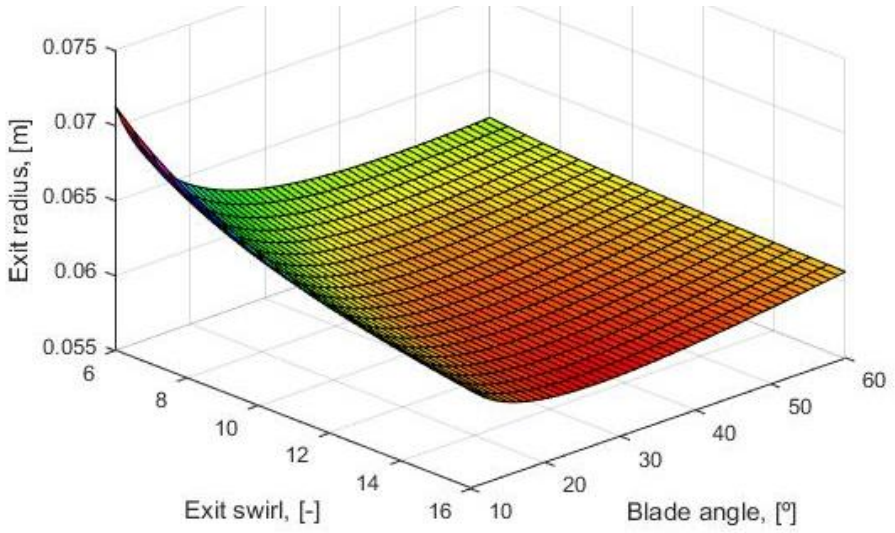

Figure 3-5: Impeller exit radius as a function of exit swirl and blade angle

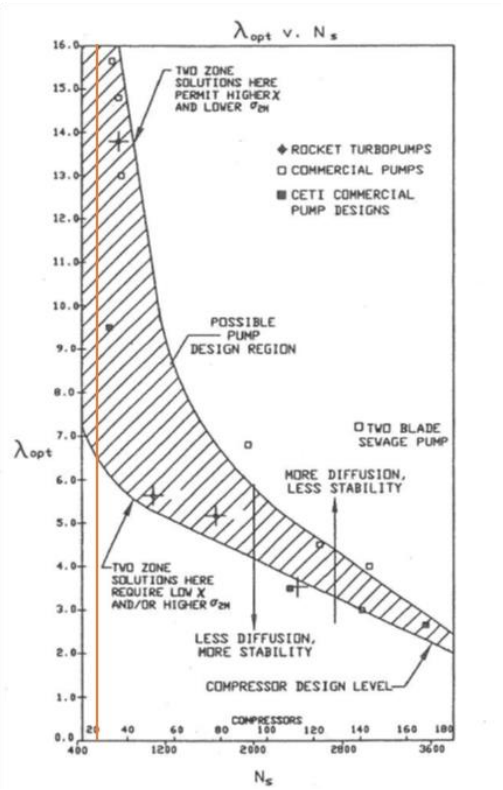

Figure 3-6: Exit swirl parameter as a function of specific speed (Japikse, et al., 2006)

It can be seen from Figure 3-5 that there exists no local minimum for the observed design space. Figure 3-7 was simultaneously generated with the data from Figure 3-5, and provides valuable insight into the meanline design space. This assists with determining the operating point of the impeller. The exit width has a distinctively linear relationship with the exit swirl parameter and is completely independent of the blade exit angle. Thus, the exit swirl parameter indirectly sets the exit width of the impeller. The available exit width ranges from 0.6 mm to 1.6 mm, approximately 1-2 % of the exit radius. These values are a concern, as flow through narrow passages is dominated by viscous effects. The governing equations, for the meanline algorithm, do not include models for boundary layer development, thus the resultant viscous losses between close proximity surfaces are not captured by the model.

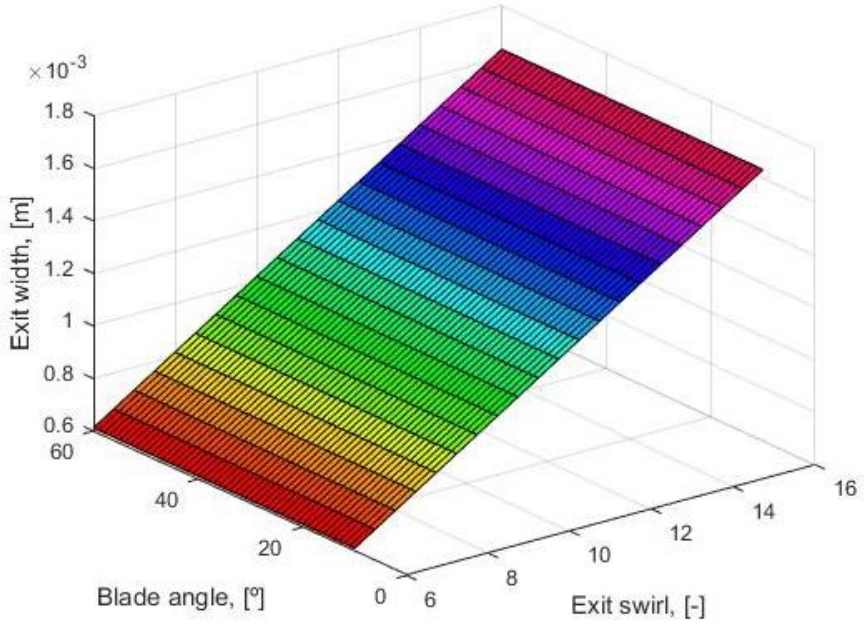

Figure 3-7: Exit width as a function of exit swirl and blade exit angle

The upper limit of the exit swirl parameter was selected. This results in a maximum exit width of 1.6 mm for the observed design space. With the exit swirl parameter now constrained, Figure 3-5 becomes two-dimensional as in Figure 3-8. The exit radius is minimised, over the constrained design space, at a blade exit angle of 29°.

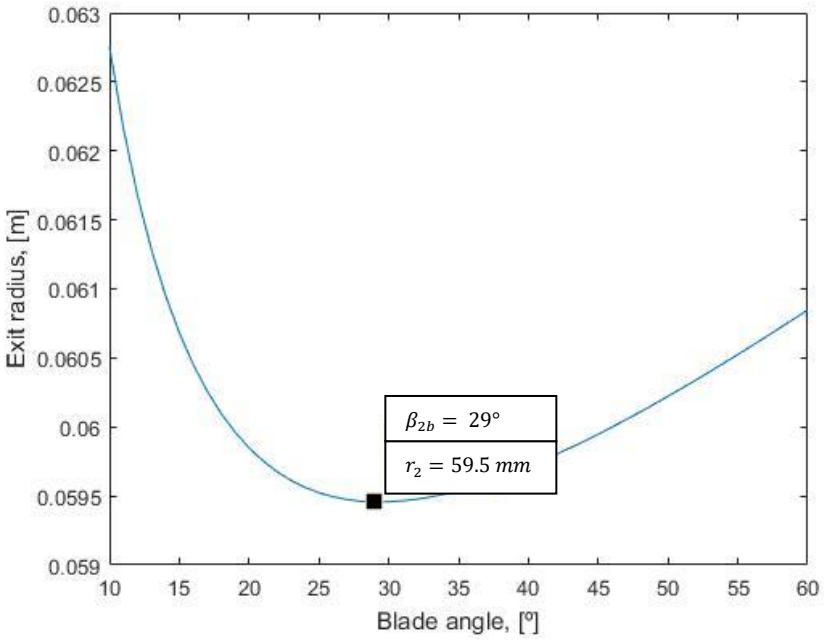

Figure 3-8: Exit radius vs blade exit angle

3.4 Vaneless diffuser

The vaneless diffuser is responsible for the recovery of the kinetic energy leaving the impeller in order to increase the static pressure; this is done by a combination of:

- Increasing the passage flow area, thus reducing the meridional velocity and increasing static pressure. The meridional velocity, at any point in the diffuser, is calculated in the same manner as Equation 3.27.
- Decreasing the tangential velocity of the fluid, by increasing the radius of the flow path. This occurs due to the conservation of angular momentum as described by Equation 3.32.

$$rC_\theta = constant \qquad [3.32]$$

Static pressure recovery is not of great importance due to the selection of a high exit swirl parameter. Sufficient diffusion occurs within the impeller passage, thus the primary purpose of the diffuser, for this pump, is to ensure adequate mixing of the low and high momentum flow regimes. Literature suggests that the flow is 90% mixed at a distance equal to 30% of the impeller exit radius, from the impeller exit (Japikse et al., 2006). Therefore, the diffuser outer radius is set to 1.3 times the impeller exit radius. The problem with the high exit swirl is

stability. To account for this, a pinch is added to the diffuser inlet as in Figure 3-9. The pinch reduces the swirl parameter in the diffuser by increasing the meridional velocity of the flow, and thus increasing the stability of the flow at the diffuser inlet. The front pinch configuration was selected for simplicity.

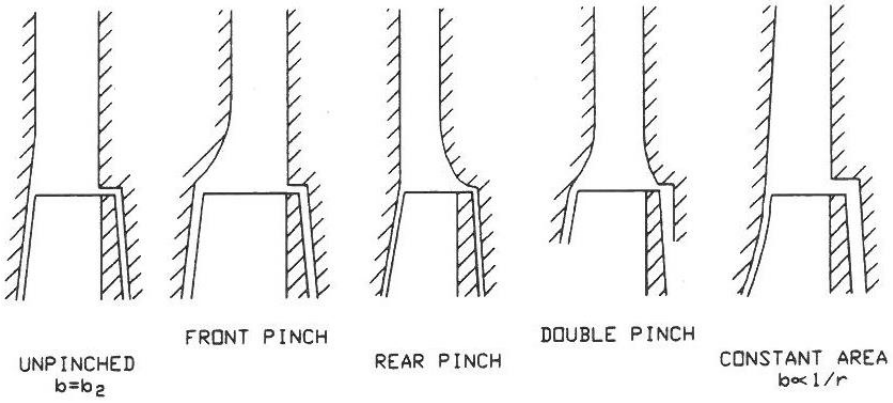

Figure 3-9: Vaneless diffuser pinch configurations (Japikse et al., 2006)

3.5 Scroll collection volute

The scroll collection volute is designed to collect the incoming radial flow for discharge into an axial conical diffuser or discharge pipe. A 2-D layout of the volute is represented in Figure 3-10. The volute should develop a constant circumferential static pressure to minimise the effect of radial loading on the impeller. This is achieved by setting the tangential velocity at the volute inlet equal to the velocity at the throat, thus there is neither acceleration nor diffusion of the flow through the volute.

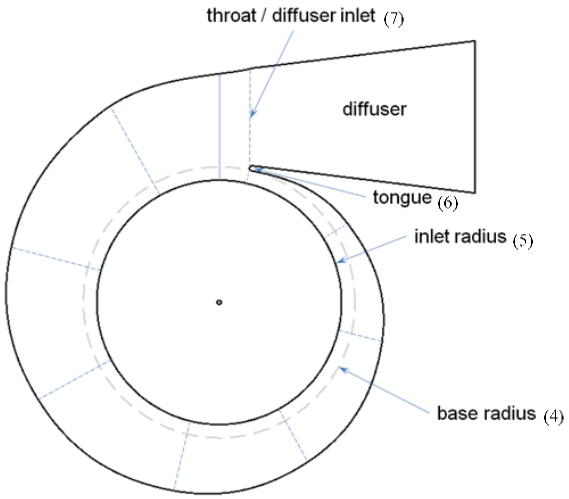

Figure 3-10 Scroll collection volute layout

The inlet swirl parameter of the volute is defined as the ratio of the tangential velocity to the meridional velocity and is represented by Equation 3.33.

$$\lambda_5 = \frac{C_{\theta 5}}{C_{m5}} \quad [3.33]$$

The area ratio of the volute throat to inlet is defined by Equation 3.34.

$$AR_7 = \frac{\pi {D_7}^2}{8\pi r_5 b_5} \quad [3.34]$$

3.6 The Barske pump

A shortcoming in the conventional impeller design is the small exit width of 1.6 mm. Even though the maximum exit width was selected, there would still be significant viscous losses within the impeller passage. The reason for this is the combination of the high head and low flowrate requirement. For conventional designs that operate at low specific speeds, the ratio of the frictional losses to the overall loss becomes large and thus unfeasible (Satoh et al. 2005). Usually this regime would suggest the use of a positive displacement pump, but for a rocket engine application, the pulsations caused by positive displacement pumps are undesirable as they may lead to "chug" instabilities within the system.

In 1950 Barske proposed an unorthodox solution to the problem of low specific speed pumps, in his (now declassified) technical report titled 'High Pressure Pumps for Rocket Motors'. Barske stated, *"To a skilled designer the pump which forms the subject of this paper will, at first glance, appear most unfavourable and may well be regarded as an offense against present views of hydrodynamics"* (Lobanoff & Ross, 1992). Figure 3-11 is a schematic of the original design presented by Barske in his technical report. The Barske pump falls into the category of a partial emission pump as the emission throat area is smaller than the impeller emission area.

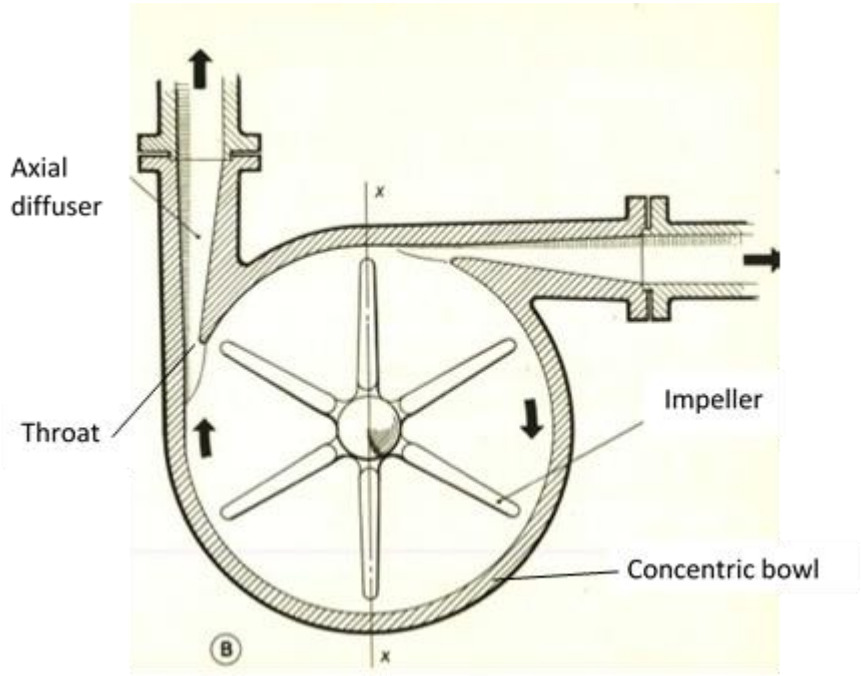

Figure 3-11: Original schematic of the Barske pump design (Barske, 1950)

A Barske pump can be identified by the characteristic open or unshrouded impeller with radial vanes, which sits within a concentrically bored bowl. The emission throat and associated conical diffuser are orientated tangentially to the bowl.

3.6.1 Barske pump operation

The fluid flow path through a Barske pump can be expressed as the superposition of two different flow fields. The first case is a non-rotating impeller; the only nett flow path available extends from the impeller inlet to the emission throat, this is due to the concentric bowl containing an incompressible fluid and thus mitigating any potential for radial flow other than that along the streamline from inlet to impeller emission area. The second flow field is set up by the rotating impeller, causing a forced vortex in the R,θ plane with high circumferential velocities. The superposition of these two fields results in a flow path that would be visually represented by a tightly wound spiral. A differential volume element would enter at the inlet and orbit around the central axis of the pump, progressively migrating to higher orbit levels until it is discharged at the throat.

Some of the advantages of the Barske impeller include reduced sensitivity to the operating clearance between the impeller and shroud, which consequently results in a simplified manufacturing process as extremely tight tolerances are not required (Barske, 1950). The open impeller style also alleviates the concern of mechanical losses through rubbing of the rotor and

casing. High quality surface finishes are unnecessary as there is minimal radial flow due to the forced vortex i.e. the low flow rate and high head characteristic only need rely on small radial velocities to meet the low flow rate requirement.

A few assumptions need to be made before performing the hydrodynamic modelling of the Barske impeller. Firstly, the generation of the forced vortex defines the impeller tangential velocity (U_θ) as a function of radial distance (r), with the angular velocity (ω) being a constant.

$$U_\theta = r\omega$$

$$\therefore \frac{\partial U_\theta}{\partial r} = \omega$$

Secondly, the radial component of velocity is neglected (i.e. approaches zero).

$$U_r = 0$$

Then from the incompressible continuity equation (Equation 3.35), it is observed that the tangential velocity does not vary with the angle position.

$$\frac{1}{r}\frac{\partial (rU_r)}{\partial r} + \frac{1}{r}\frac{\partial U_\theta}{\partial \theta} = 0 \qquad [3.35]$$

$$\therefore \frac{\partial U_\theta}{\partial \theta} = 0$$

The steady state Navier-Stokes equations (in cylindrical coordinates) can now be used to determine the pressure field, starting with the tangential component in Equation 3.36.

$$\rho\left(U_r\frac{\partial U_\theta}{\partial r} + \frac{U_\theta}{r}\frac{\partial U_\theta}{\partial \theta} + \frac{U_r U_\theta}{r}\right) = -\frac{1}{r}\frac{\partial P}{\partial \theta} + \mu\left[\frac{1}{r}\frac{\partial}{\partial r}\left(r\frac{\partial U_\theta}{\partial r}\right) - \frac{U_\theta}{r^2} + \frac{1}{r^2}\frac{\partial^2 U_\theta}{\partial \theta^2} - \frac{2}{r^2}\frac{\partial U_r}{\partial \theta}\right] \qquad [3.36]$$

$$\therefore \frac{\partial P}{\partial \theta} = \mu\left[\frac{1}{r}\omega - \frac{\omega}{r}\right]$$

$$\therefore \frac{\partial P}{\partial \theta} = 0$$

The solution of the above Navier-Stoke equation indicates that there is no relationship between the pressure and the observed angle, thus the following statement can be made,

$$P = f(r, \theta) \rightarrow P = f(r)$$

Next the radial component is solved.

$$\rho\left(U_r \frac{\partial U_r}{\partial r} + \frac{U_\theta}{r}\frac{\partial U_r}{\partial \theta} - \frac{{U_\theta}^2}{r}\right) = -\frac{\partial P}{\partial r} + \mu\left[\frac{1}{r}\frac{\partial}{\partial r}\left(r\frac{\partial U_r}{\partial r}\right) - \frac{U_r}{r^2} + \frac{1}{r^2}\frac{\partial^2 U_r}{\partial \theta^2} - \frac{2}{r^2}\frac{\partial U_\theta}{\partial \theta}\right] \quad [3.37]$$

$$\therefore \frac{\partial P}{\partial r} = \rho\frac{{U_\theta}^2}{r}$$

Solving the partial differential equation above gives an explicit definition of the total pressure as a function of radial distance.

$$\int_{P_1}^{P_2} \partial P = \rho\omega^2 \int_{r_1=0}^{r_2} r\,\partial r$$

$$\therefore \Delta P_{static} = \rho\frac{{U_{\theta 2}}^2}{2}$$

Therefore, the total head rise across the pump is defined by Equation 3.38.

$$\Delta P_{total} = \Delta P_{static} + \Delta P_{dynamic}$$

$$\Delta P_{total} = \rho\frac{{U_{\theta 2}}^2}{2} + \left(\rho\frac{{U_{\theta 2}}^2}{2} - 0\right)$$

$$\therefore \Delta H_{total} = \frac{{U_{\theta 2}}^2}{g} \quad [3.38]$$

Equation 3.38 is an attempt at describing the total, theoretical head rise across the impeller. The actual head rise is defined in the same manner with the inclusion of a head coefficient (ψ), as seen in Equation 3.39. The subscript indicating the tangential velocity component is now dropped, as it only served as a reference during the solution of the Navier-Stokes equations. The velocity term in Equation 3.39 is representative of the impeller tip speed, and not the actual tangential velocity of the flow; the values do however equate under no slip conditions.

$$\therefore \Delta H_{total} = \psi \frac{{U_2}^2}{g} \quad [3.39]$$

3.6.2 Barske design

The inlet design of the Barske impeller usually consists of straight radial vanes in a two-dimensional (R, θ) plane, thus having a radial inlet as in Figure 3-11. In this study, however, a conventional inlet design approach was adopted. This was to improve inlet performance by attempting to guide the flow smoothly from an axial to radial orientation. Thus, the inlet design of the impeller follows the same design procedure as the conventional pump. The operating speed of the Barske pump is determined using the same process presented by Figure 3-4.

Equation 3.39 can be restructured to form Equation 3.40, from which the impeller diameter can be obtained.

$$U_2 = \frac{\pi D_2 N}{60}$$

$$\Delta H_{total} = \psi \frac{\pi^2 (D_2 N)^2}{60^2 g}$$

$$D_2 = \frac{1}{N} \sqrt{\frac{\Delta H}{\psi} \left(\frac{60^2 g}{\pi^2} \right)} \quad [3.40]$$

A head coefficient (ψ) of 0.74 has been deemed acceptable through experimental testing (Lobanoff and Ross, 1992).

Equation 3.41 defines the flowrate at the emission throat by determining the throat velocity and multiplying by the throat area (which is designed to be circular). The throat velocity is embedded in the flow coefficient (ϕ) which is a ratio of the meridional throat velocity to impeller tip speed. The flow coefficients for partial emission pumps are found to be near 0.8 (Lobanoff & Ross, 1992).

$$Q = \phi U_2 A_t \quad [3.41]$$

The emission throat diameter can be found by substituting Equation 3.39 into Equation 3.41 to form Equation 3.42.

$$Q = \phi \sqrt{\frac{Hg}{\psi}}\, \pi (r_{throat})^2$$

$$\therefore D_{throat} = 2\sqrt{\frac{Q}{\varphi\pi}\sqrt{\frac{\psi}{Hg}}} \quad [3.42]$$

The conical diffuser, after the throat, can be set to any reasonable length, although a 10° divergence angle is suggested for optimal diffusion (Barske, 1950). Using basic trigonometry, the diffuser length (l_d) is calculated as per Equation 3.43.

$$l_d = \frac{r_{exit} - r_{throat}}{\tan(10°)} \quad [3.43]$$

3.7 Conclusion

This chapter dealt with developing an appropriate conventional impeller design, by utilizing meanline pump characteristics to generate a design that satisfied the objective of minimising pump weight by maximising impeller speed. A novel algorithm was developed to determine the maximum allowable impeller speed based on cavitation parameters suggested by literature. The exit parameters are found by implicitly solving a single governing equation (Equation 3.30), with the solution of the equation being sufficient to describe all other exit parameters. The problem with the conventional design is the excessively narrow flow passages because of the

low specific speed. This causes degraded pump performance due to the disproportionately high losses. An appropriate analogy to explain the disproportion in losses, is the hydrodynamics of pipe flow. The skin friction in a pipe is dependent upon the wetted area, that is the circumference of the pipe, and thus can be viewed as proportional to the pipe diameter. The flow through the pipe is proportional to the cross-sectional area of the pipe and is therefore proportional to the square of the diameter. Figure 3-12 illustrates the above statement by representing the loss associated with skin friction as a ratio to the overall throughput of the flow plotted against varying pipe diameters.

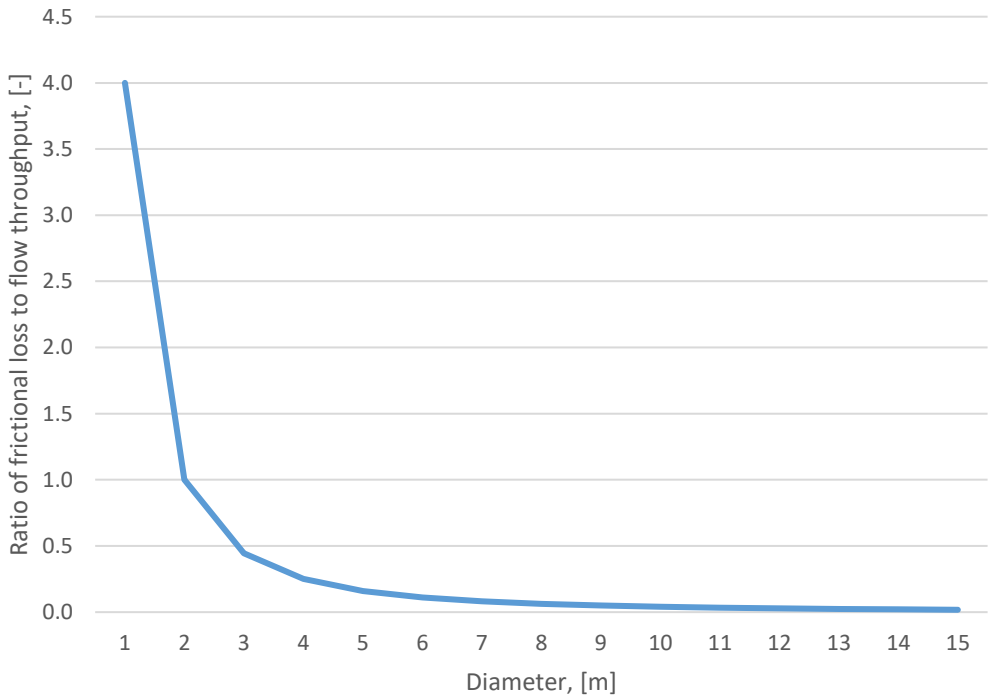

Figure 3-12: Ratio of skin friction loss to flow throughput as a function of pipe diameter

The problem of the low specific speed pump, with narrow passageways, was dealt with by using a partial emission pump, specifically the Barske pump design. The Barske pump uses an open impeller, in a concentric bowl, to create a forced vortex. The equation representing the static pressure within the forced vortex is derived from the polar form of the Navier-Stokes equations. Table 3-2 lists the resultant conventional design parameters with the impeller geometry seen in Figure 3-13. The Barske design parameters are listed in Table 3-3 with the impeller geometry displayed in Figure 3-14.

Table 3-2: Parameters for conventional impeller design

Speed	22850 rpm
Inlet hub radius	6.6 mm
Inlet tip radius	10.8 mm
Inlet blade angle	33.99° ≅ 34°
Exit blade angle	29°
Exit width	1.6 mm
Exit radius	59.46 mm
Shroud clearance	0.5 mm
Blades	7

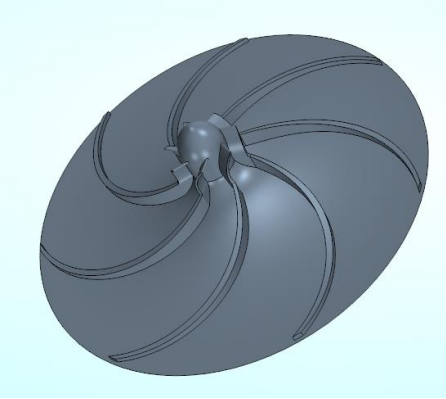

Figure 3-13: Conventional design impeller geometry

Table 3-3: Parameters for Barske impeller design

Speed	22850 rpm
Inlet hub radius	6.6 mm
Inlet tip radius	10.8 mm
Inlet blade angle	33.99° ≅ 34°
Exit blade angle	90°
Exit width	7.5 mm
Exit radius	41.5 mm
Shroud clearance	0.5 mm
Primary blades	8
1st splitter set	8
2nd splitter set	16

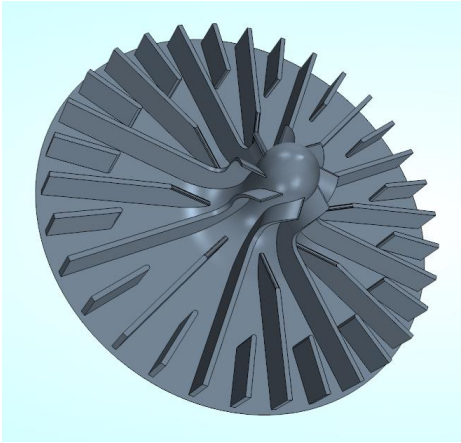

Figure 3-14: Barske impeller design

Both designs must undergo CFD analyses to evaluate their respective performances. The meanline algorithms used to develop these designs, are a starting point. In the sections that follow, the designs are refined through the analysis of their respective flow fields to ensure that they meet the hydrodynamic system requirements. Any efficiency optimization can only be done by using CFD techniques, as there is no adequate way to analytically model the flow field of such a turbulent three-dimensional flow process.

4. CFD Analysis and Design Enhancement

4.1 Introduction

CFD techniques involve numerically solving the partial differential equations that describe real flows, as they cannot be solved analytically for complex geometries. In the present study, they are used to evaluate the performance of the pump designs under a set of initial conditions. The CFD codes are solved to varying degrees of accuracy due to the errors that arise during the discretization of the analytical equations. It is for this reason that the CFD solution cannot be claimed to be an identical description of the flow in reality. Well-developed CFD codes provide a quick and cost-effective means of approximately evaluating the flow field; this information can then be used to make informed, and quick design changes (Ucer, 1994). For a design engineer the issue of uniformity amongst simulations is stressed by Tsuei (2001). There should be no adjustment of CFD parameters or selected models between simulations. A consistent set of modelling parameters are to be used for designs undergoing comparative analysis. The software package used for the simulations in this chapter was STAR CCM+™, V12.04.

4.2 CFD turbulence model selection

Most CFD solvers are based on the Reynolds-averaged Navier-Stokes equations. These equations pose a closure problem due to turbulence. This is dealt with by turbulence models, which are additional empirical equations to represent the velocity fluctuations, caused by turbulence, and hence close the equation set. All turbulence models are empirically derived (Gülich, 2007). They contain models with constants that are adjusted so the CFD result matches the real-world flow as closely as possible.

The k-ε model is the standard two-equation turbulence model which is based upon the specific kinetic energy (k) and a dissipation rate (ε) of the turbulence. Alone, the k-ε model is insufficient to capture flow phenomena through some of the simplest components, such as diffusers and bends. It was therefore concluded by Gulich (2007), that it is unsuitable for the calculation of flow fields in pumps. The k-ω model deals with some of the shortcomings of the k-ε model as it was developed specifically for flows against strong pressure gradients. It deals with the flow near the wall much better than its counterpart, which handles the flow in the core region with greater accuracy. The k-ω model still struggles to deal with the effects of flow separation. The shear stress transport model (SST) employs the k-ε model, in the core region of

the flow, and the *k-ω* model near the surfaces. It contains additional empirical functions for the transition between the two models.

Mao et al. (2014) tested the accuracy of four turbulence models employed to simulate the flow through a volute type pump. The models being tested included the standard *k-ω* model, the SST *k-ω* model and two variations of the *k-ε* model. The results showed that the SST *k-ω* model was the most accurate, as it matched the developed head of the physical experiment with the least amount of error. Hedi et al. (2012) used the SST *k-ω* model in their simulations to investigate the flow structure through centrifugal pumps, as did Ren et al. (2016) in their work trying to improve the turbulence model in regions of flow separation.

The SST has been deemed the most appropriate model available for pumps by Gülich (2007). An all *y+* wall treatment was used for the following simulations, this incorporates both linear and logarithmic wall functions, thus wall *y+* values may range from 0 to 300.

4.3 Design analysis

Both the conventional and Barske impellers were analysed and the results are presented below. This was done using identical physics models. The flow domains were created using a CAD package and imported into STAR CCM+™.

4.3.1 Model setup

The flow domains are broken down into three regions, ‘A’, ‘B’, and ‘C’ as seen in Figure 4.1. Region A is the inlet duct flow domain and extends to the rotor inlet. This marks the start of region B, which is specified as a rotating reference frame, consisting of either the conventional or Barske impeller. For the conventional design, region C consists of the radial diffuser, scroll collection volute and conical diffuser flow domains; while for the Barske design it is just the concentric bowl and conical diffuser.

The boundary conditions are identical for each model. The inlet boundary is stipulated as a pressure inlet and has a total pressure of 3 bar prescribed to it. Literature suggests a low tank pressure is desirable to minimize the overall weight of the rocket (Huzel and Huang, 1992). In conventional turbopump, systems higher tank pressures require stronger tanks, hence more material is used and thus the rocket becomes heavier. The propellant tanks on the space shuttle main engine were pressurised to a value of 2.3 bar (NASA, 1988).

The outlet boundary (at the end of the conical diffuser) is set as a mass flow outlet of 2.75 kg/s. The pressure at the outlet face is then used as a measure of convergence. All other surfaces in the flow domain are defined as non-slip walls.

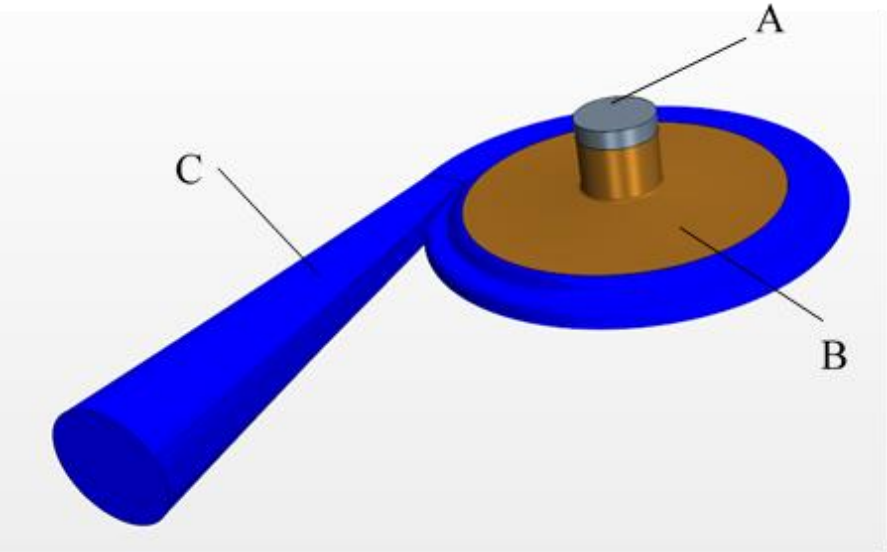

Figure 4-1: Region definition for CFD model

4.3.2 Mesh independence

The accuracy of CFD simulation depends on a number of parameters, such as the model selection, boundary conditions and quality of mesh. Mesh independence attempts to mitigate the cell number as a variable in the CFD solution. This is done by creating progressively finer meshes while observing the variation in the output parameter of interest. In this case it is the static pressure value at the outlet of the conical diffuser.

The results of the mesh independence study are displayed in Figure 4-2 and Figure 4-3. The first of the two figures shows that mesh independence, for the conventional design, occurs between a mesh size of approximately 1 750 000 and 3 200 000 cells. For the Barske design, mesh independence is found between 1 300 000 and 5 550 000 cells. Finding the exact cell number, at which mesh independence occurs, is not a feasible process from a temporal perspective, thus the upper limit of each aforementioned interval is used for the respective designs. This ensures the simulation is running at a cell count beyond the mesh independence threshold.

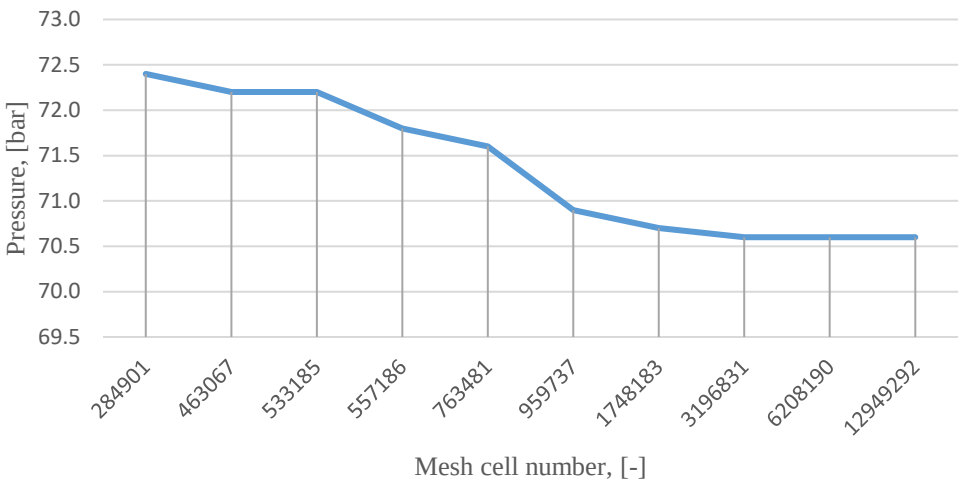

Figure 4-2: Mesh independence for conventional design

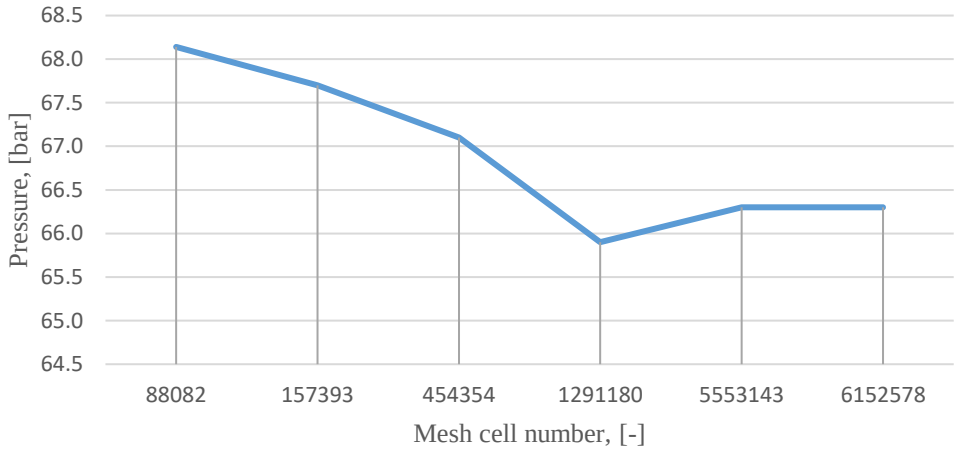

Figure 4-3: Mesh independence for Barske design

4.3.3 Results

Both designs did not meet the hydrodynamic requirements set in the meanline system (Section 2.6) to the desired level of accuracy, however this was anticipated from the first design iteration. The meanline design process generated a baseline design which can be refined through an iterative process by tweaking the design parameters based on information observed from the CFD analysis.

The easiest parameter to alter (within the CFD software package) is the operating speed of the impeller. This allows for a suitable design to be obtained in the shortest amount of time. The speed from the meanline design was 22 850 rpm, this value was iteratively altered to achieve an

acceptable head rise across the pump. The adjusted speeds and results can be found in Table 4-1. The hydraulic efficiency is calculated as per Equation 4.1

$$\eta_H = \frac{\rho g Q H}{T \omega} \quad [4.1]$$

where the torque (T) is determined by summing the shear and static pressure force, on each discretized element, across the impeller and shroud surface.

Table 4-1: Comparative analytical results from CFD analysis

	Conventional design	**Barske design**
Initial speed	22850 rpm	22850 rpm
Pressure output at initial speed	70.6 bar	66.3 bar
Corrected speed	21490 rpm	22050 rpm
Pressure output at corrected speed	61.9 bar	61.8 bar
Hydraulic efficiency	54.3%	63.6%
Power	36.5 kW	31 kW
Radial load	166.9 N	469.8 N

From the favourable performance results obtained, the Barske design was selected for further development. This was due to the greater efficency potential and reduced power requirement (the simulation only provides an approximation of the pump efficency and power demand). The conventional design's static pressure, absolute velocity and cell relative velocity fields can be found in Appendix C.

The static pressure field of the Barske design is illustrated by Figure 4-4. The extended dark-blue region (circled in red on Figure 4-4) is indicative of a non-axisymmetric, low pressure zone which is a result of the adjacent "draw-off" of fluid and its acceleration toward the nearby conical diffuser inlet (circled in red on Figure 4-5). It is also indicative of an induced radial load on the impeller shaft, which is significantly higher than in the conventional design. As a result of this, a hybrid design between the conventional and Barske design was considered in an attempt to develop a pump that mantains the efficency of the Barske design but has a reduced radial load. The hybrid design is described in the section that follows. From Figure 4-4 it is clear the Barske concentric bowl plays an insignificant roll in pressure recovery with the process being entirely attributed to the concical diffuser.

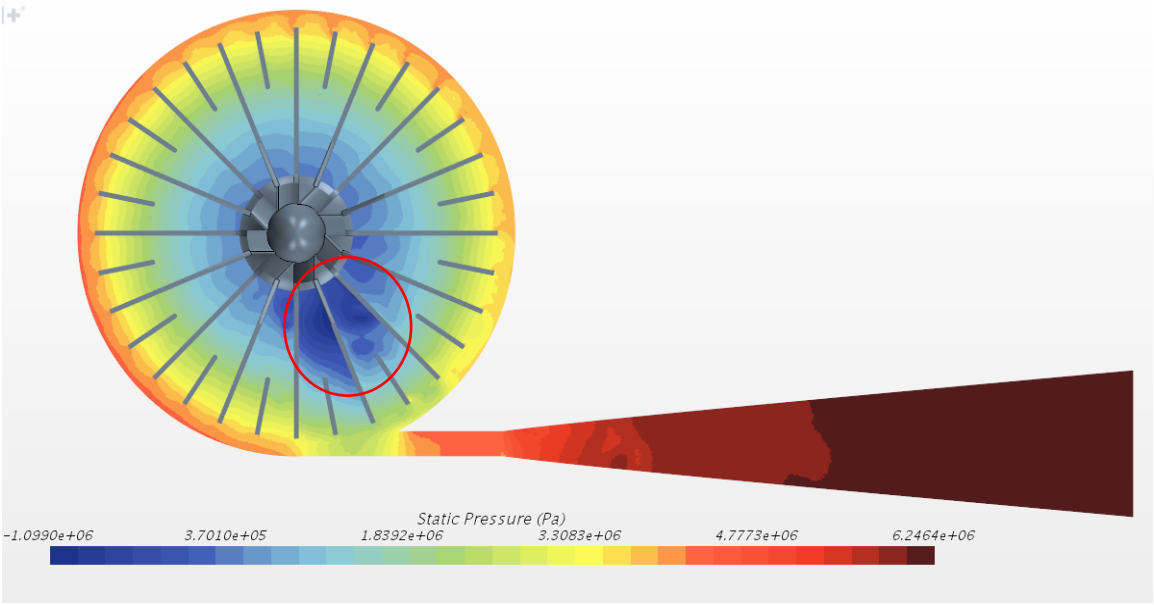

Figure 4-4: 2D cross section of the static pressure field in the Barske design

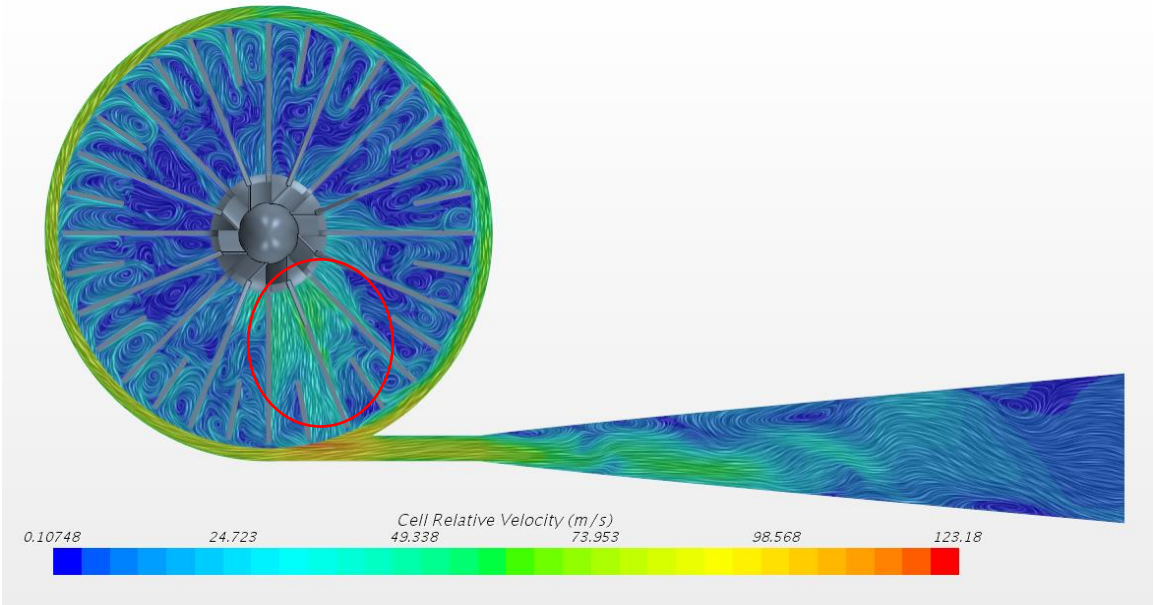

Figure 4-5: 2D cross section of the relative velocity field in the Barske design

4.4 Hybrid design

A proposed solution to the problem of the non-axisymmetric pressure field, is to use a scroll collection volute. As in the conventional design, the scroll collection volute serves to collect the flow and maintain an essentially constant circumferential pressure that minimises radial loading. Figure 4-6 depicts the radial loading profiles induced by each collector type. Radial loading is minimized when operating at the design point using a scroll collection volute.

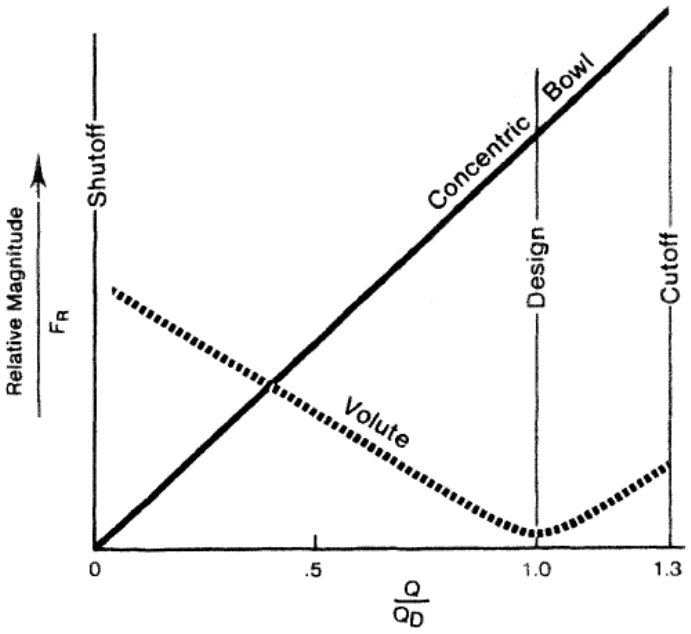

Figure 4-6: Comparative radial loading between a concentric bowl and inlet to the volute for various fractions of design flow rate (Lobanoff and Ross, 1992)

The pump configuration, consisting of a Barske impeller and scroll collection volute, is referred to as the hybrid design. The static pressure and relative velocity fields, of the hybrid design, are illustrated in Figure 4-7 and Figure 4-8 respectively. Table 4-1 is replicated as Table 4-2 with the addition of the hybrid design's results. Immediately noteworthy is that in all cross-sectional views of the flow field data is drawn from a mid-plane i.e. R, θ at half exit blade height.

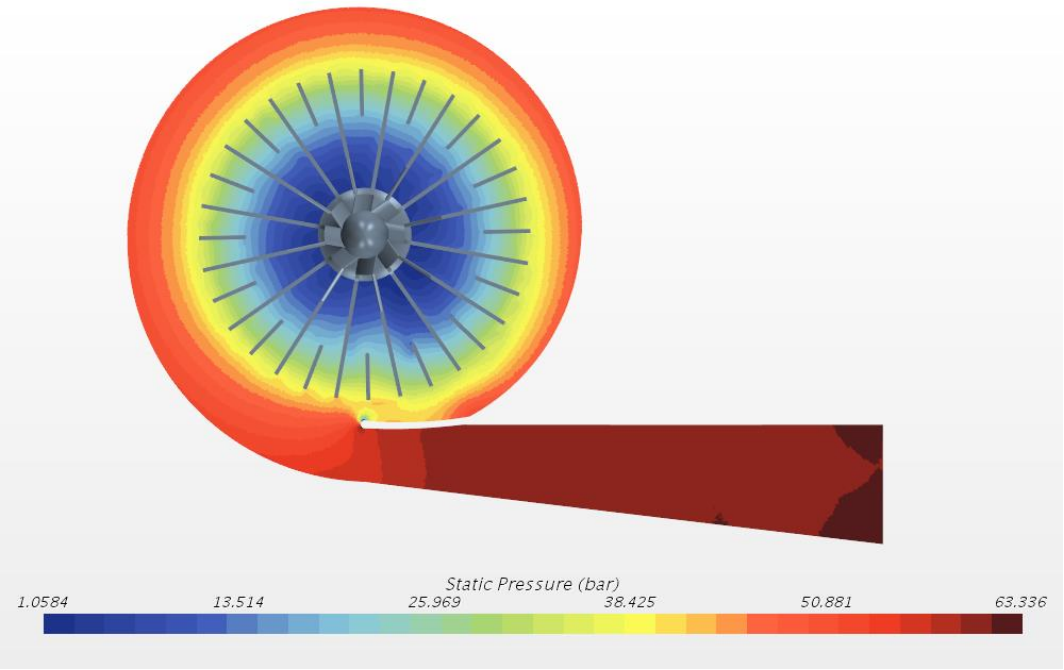

Figure 4-7: 2D cross section of the static pressure field in the hybrid design

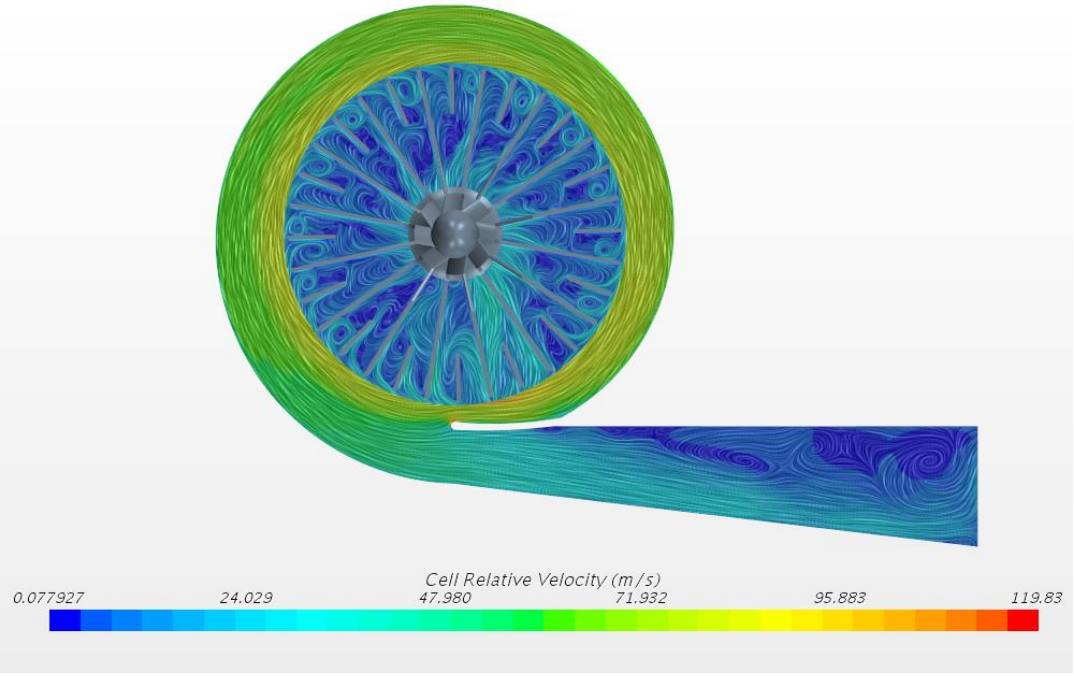

Figure 4-8: 2-D cross section of the relative velocity field in the hybrid design

Table 4-2: Comparative analytical results including hybrid design

	Conventional design	Barske design	Hybrid design
Initial speed	22850 rpm	22850 rpm	22850 rpm
Pressure output at initial speed	70.6 bar	66.3 bar	64.2 bar
Corrected speed	21490 rpm	22050 rpm	22300 rpm
Pressure output at corrected speed	61.9 bar	61.8 bar	61.8 bar
Hydraulic efficiency	54.3%	63.6%	62.6%
Power	36.5 kW	31 kW	31.6 kW
Radial load	166.9 N	469.8 N	138.6 N

The hybrid design is 1 % less efficient than the Barske design, however, it has a greater degree of axisymmetry. This can be observed visually by comparing the pressure fields in Figure 4-4 and Figure 4-7. Quantitatively, it is reflected in the reduction of the nett radial force from 469.8 N to 138.6 N.

The steady state analysis of the hybrid design cannot simulate the phenomena of cavitation; however, it can provide an indication of where the working fluid may cavitate. Figure 4-9 represents the potential areas of cavitation inception, by mapping an iso-surface of RP-1's vapour pressure (2275 Pa at standard temperature). To determine the severity of the cavitation, a transient analysis with a multiphase physics model is required. This was beyond the scope of the present study

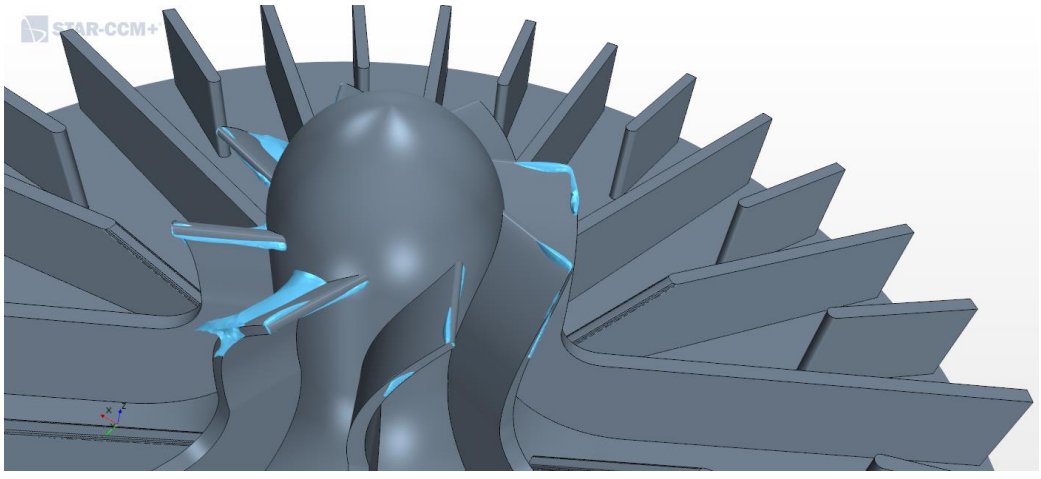

Figure 4-9: Iso-surface of RP-1 vapour pressure

4.5 Conclusion

A CFD analysis was performed on the geometric flow domains, generated from the conventional and Barske meanline design algorithms. The Barske design demonstrated a greater efficiency potential than the conventional design, this was due to the disproportionately high losses occurring in the conventional impeller passageways (as discussed in section 3.3). The Barske design exhibited an uneven pressure distribution about the axis of rotation, consequently inducing a nett radial thrust of circa 469.8 N on the impeller drive shaft. The concentric bowl was replaced with a scroll collection volute to evenly distribute the circumferential pressure around the Barske impeller. The resulting pressure field caused a reduction in the nett radial force by a factor of approximately 4.5. The steady state analysis indicated areas likely to be prone to cavitation inception along the leading edges of the impeller blades. The cavitation on the pump inlet needs to be mitigated to attain acceptable results and as will be shown later, raising the fuel tank pressure from 3 bar to 9 bar is considered a potential solution path albeit achieved with possibly increased tank weight.

5. The Effect of Changing Tank Pressure on Vehicle Mass

5.1 Introduction

The impeller design algorithm was intended to mitigate cavitation as described in section 3.2.3. However, the cavitation model used in the meanline algorithm is overly simplified and fails to factor in the effects of surface roughness, inlet blade profile and dynamic fluid blockage. The suggested presence of cavitation in the CFD analysis, of the hybrid design, brings into question the validity of the claimed efficiency. The analysis does not model the phase change or the propagation of the bubbles. Cavitation should be completely mitigated to attain a reliable result from the steady state analysis.

The problem of cavitation can be resolved in one of two ways; the addition of an inducer or an increase in the total inlet pressure. Inducers are essentially axial flow machines positioned upstream of the centrifugal impeller. They slightly raise the pressure of the incoming flow to allow the main impeller to operate without the onset of cavitation. Most inducers operate with varying degrees of cavitation but are able to distribute the collapsing of bubbles over a larger blade area, thus preventing localized surface impingement (Karassik et al., 1986). Adding an inducer raises the overall vehicle mass but only by the weight of the inducer itself.

Mass models were developed to compare the viability of increasing the propellant tank pressure in comparison to the addition of an inducer.

5.2 Mass models

A viable tank pressure is defined as being greater than, or equal to, the threshold pressure at which cavitation no longer occurs, as well as ideally resulting in a nett mass change of the vehicle that does not exceed the mass of an inducer. The optimal tank pressure would be a value greater than, or equal to the threshold pressure and results in the lowest, nett mass gain of the vehicle (or the greatest reduction in vehicle mass).

The mass models presented in this chapter also investigate the appropriateness of the suggested 3 bar tank pressure by Huzel and Huang (1992) and Sutton and Biblarz (2001).

5.2.1 Tank mass

Any increase in tank pressure requires a thicker walled pressure vessel, consequently adding unwanted mass to the vehicle. Modern propellant tanks are manufactured from composite materials, for example Electron utilizes carbon composites for the propellant tanks. The Phoenix 1-B hybrid rocket, currently being developed by ASReG, will make use of a Carbon T300/Epoxy, filament wound oxidiser tank. The approximate thickness of the composite tank may be calculated from Equation 5.1 (Kabir, 2000);

$$t_{tank} = \frac{P_{tank} r_{tank}}{\Theta_{tank}} \left(1 - \frac{tan^2 \delta}{2} + \frac{1}{2cos^2 \delta}\right) \quad [5.1]$$

where (Θ_{tank}) is the yield stress of the tank composite material. For a winding angle (δ) of 60°, the change in wall thickness (Δt_{ct}) can be represented as a function of the changing tank pressure:

$$\Delta t_{tank} = \frac{\Delta P_{tank} r_{tank}}{\Theta_{tank}} (1.5) \quad [5.2]$$

The additional tank mass is determined by multiplying the change in volume of the tank by the material density as per Equation 5.3.

$$\Delta m_{tank} = \pi((r_{tank} + \Delta t_{tank})^2 - {r_{tank}}^2) l \rho_{tank} \quad [5.3]$$

Substituting Equation 5.2 into Equation 5.3 results in Equation 5.4.

$$\Delta m_{tank} = f(\Delta P) = Z\left(3\Delta P + \frac{\Delta P^2}{\Theta_{tank}}\right) \quad [5.4]$$

where,

$$Z = l \rho_{tank} \left(\frac{\pi {r_{tank}}^2}{\Theta_{tank}}\right)$$

The increasing tank pressure reduces the fuel requirement in the turbopump system, this causes a reduction in the propellant tank volume, and consequently reduced tank mass (the mass change due to a reduction in fuel is discussed in the following section). The change in tank mass due to the fuel reduction is described by Equation 5.5 where *l* is the tank length.

$$\Delta m_{tank1} = \frac{(\Delta m_f)\,(\Delta m_{tank})}{(\rho_f)\pi\,({r_{tank}}^2)\,(l)} \quad [5.5]$$

5.2.2 Fuel/battery mass

Increasing the tank pressure reduces the hydraulic power requirement on the pump. In the case of the turbopump, the amount of fuel needed to drive the pump is reduced; while in the electropump case the battery mass is reduced. The change in the hydraulic power requirement is described by Equation 5.6.

$$\Delta Hydraulic\ power = -Q(\Delta P) \quad [5.6]$$

The change in mass of the fuel/battery is the product of the change in hydraulic power with the burn time, divided by the appropriate specific energy and efficiency values. The specific energy of fuel is 2126.43 kJ/kg and 468 kJ/kg for lithium-polymer batteries (Tacca, 2010). Equation 5.7 represents the change in mass of the fuel/battery.

$$\Delta m_{fuel/battery} = \frac{\pi {r_{tank}}^2 l}{\eta_x \varepsilon_x}\left(\frac{P_{req} - (P0 + \Delta P)}{\eta_h} - \frac{P_{req} - P0}{\eta_{h0}}\right) \quad [5.7]$$

where,

$\eta_h = f(\Delta P)$

η_{h0} = Hydraulic efficiency evaluated at initial inlet pressure

$P0$ = Initial fuel tank pressure

For the turbopump case:

ε_x = Specific energy of fuel

η_x = Turbine and mechanical efficiency

For the electropump case:

ε_x = Specific energy of battery

η_x = Product of battery and motor efficiency

The product of the overall turbine and mechanical efficiency is set to 0.65 (Fitzgerald, 2015) while the battery and motor efficiencies are presumed to be 0.95 and 0.9 respectively (Tacca, 2010).

The pump hydraulic efficiency is a multi-variate function, but for the purposes of this investigation only the relationship between the hydraulic efficiency and inlet pressure is of interest. The function is derived from a set of discrete data points assimilated from multiple CFD simulations. The third order polynomial regression line, in Figure 5-1, represents the trend of the hydrodynamic pump efficiency as a function of inlet pressure.

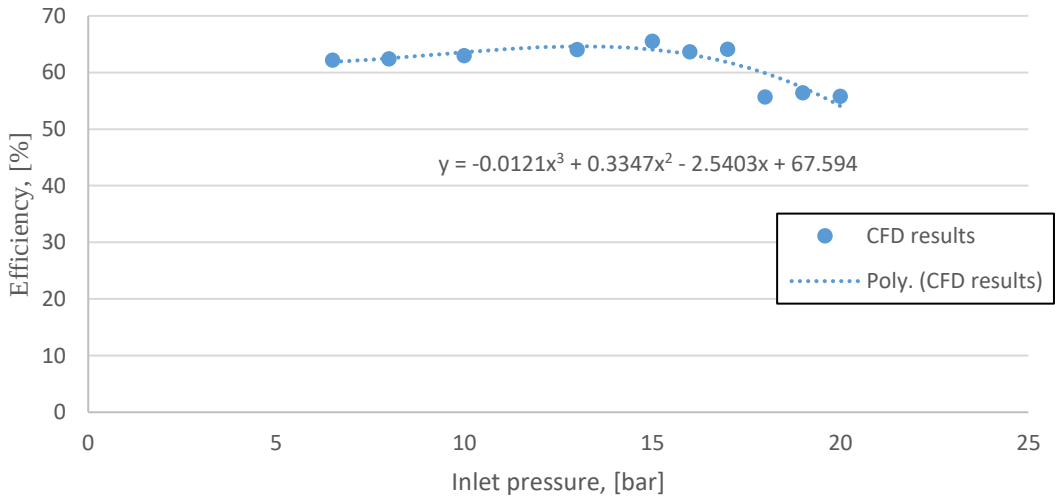

Figure 5-1: Polynomial regression line for pump efficiency as a function of inlet pressure

5.2.3 Pressurization Tank

The propellant tanks are connected to a pressurization system that uses an inert gas to maintain the desired tank pressure. This model uses helium as the pressurant which is stored in spherical tanks with a volume equal to 10% of the fuel tank volume (Hermsen, 2017). The mass of helium required (m_{helium}) can be calculated from Equation 5.8 which is based upon the ideal gas law:

$$m_{helium} = \frac{1.1(\pi)({r_{tank}}^2)(l)P_{tank}}{(\bar{R})(T)} \quad [5.8]$$

where, the specific gas constant $\bar{R}$ = 2077 J·kg^{-1}·K^{-1} and standard temperature is used. To determine the weight of the pressurant tank the required initial pressure (P_i) needs to be known so that the wall thickness may be determined. Once again using the ideal gas law the initial pressure is calculated as per Equation 5.9.

$$P_i = \frac{m_{helium}(\bar{R})(T)}{0.1(\pi)({r_{tank}}^2)(l)} = 11(P_{tank}) \quad [5.9]$$

The spherical tank material is presumed to be manufactured from the same material as the propellant tanks, thus the same representative yield strength is used. Equation 5.10 is used to determine the required thickness of the tank:

$$t_h = \frac{(P_i)(r_{tank})}{2\Theta_{tank}} \quad [5.10]$$

where, t_h is the wall thickness of the spherical tank. The mass of the pressurant tank (m_{helium_tank}) is then calculated by Equation 5.11.

$$m_{helium\_tank} = \frac{4}{3}\pi((r_{tank} + t_h)^2 - (r_{tank})^2)\rho_{tank} \quad [5.11]$$

5.2.4 Results

The turbopump mass model (Equation 5.12) is the sum of the increased tank mass due to increased pressure (Δm_{tank}), the change in the mass of fuel being carried (Δm_{fuel}), the change in tank mass due to decreased fuel volume (Δm_{tank1}), the change in mass of helium needed for pressurization (Δm_{helium}) and the change in mass of the spherical helium tank (Δm_{helium_tank}).

$$\Delta m_{vehicle} = \Delta m_{tank} + \Delta m_{fuel} + \Delta m_{tank1} + \Delta m_{helium\_tank} + \Delta m_{helium} \quad [5.12]$$

On the other hand, the change mass of a vehicle using an electropump system is described by Equation 5.13.

$$\Delta m_{vehicle} = \Delta m_{tank} + \Delta m_{battery} + \Delta m_{helium\_tank} + \Delta m_{helium} \quad [5.13]$$

The models are applied to launch vehicles of varying sizes. The size of the vehicle is defined as the volume of fuel being carried. Using a fixed aspect ratio, the tank dimensions are applied to the mass models for varying tank lengths. Figure 5-2 demonstrates the effect that changing tank pressure has on the nett change in vehicle mass, for vehicles of different sizes that make use of a turbopump system. It can be seen that the penalty for increasing the tank pressure is less severe for smaller sized vehicles, thus justifying the use of blowdown systems for small scale vehicles. For larger vehicles, increasing the tank pressure has a detrimental effect on the vehicle mass, thus the recommendation of a relatively low tank pressure, allowing the turbopump to generate the necessary head rise. To mitigate cavitation, in a relatively large vehicle utilizing a turbopump system, an inducer is the only viable option.

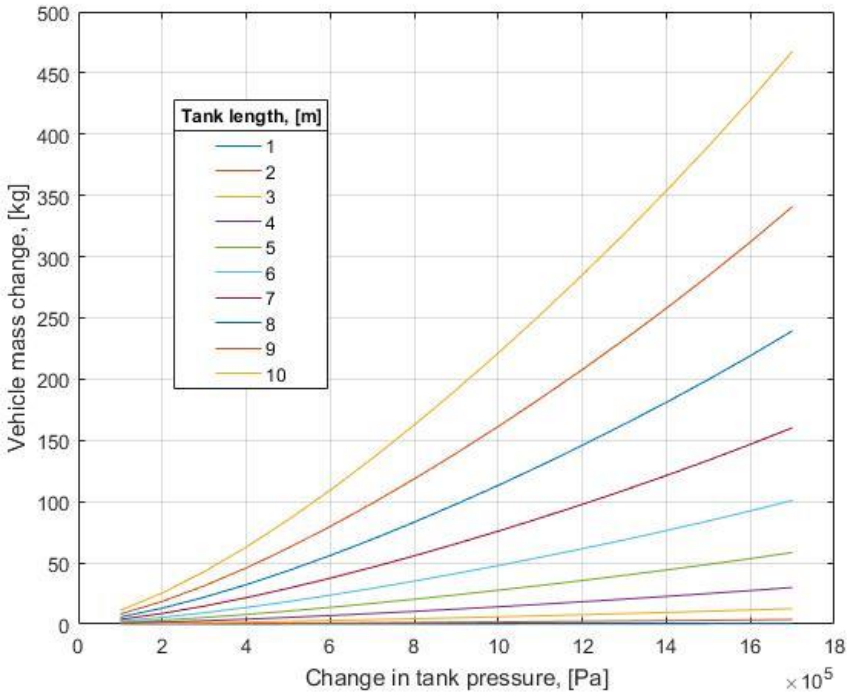

Figure 5-2: Change in vehicle mass as a function of the change in tank pressure (relative to 3 bar) for varying sized vehicles utilizing a turbopump system

Figure 5-3 is the equivalent mass model for the electropump system. As in the case of the turbopump, the mass of smaller sized vehicles is not strongly dependent on the changing tank pressure. There is a nett reduction in vehicle mass with increasing tank pressure up to an increase of 6 bar (9 bar absolute tank pressure), thereafter the vehicle mass steadily increases. This suggests an optimal tank pressure of 9 bar for all vehicle sizes (that use an identical chamber pressure to SAFFIRE).

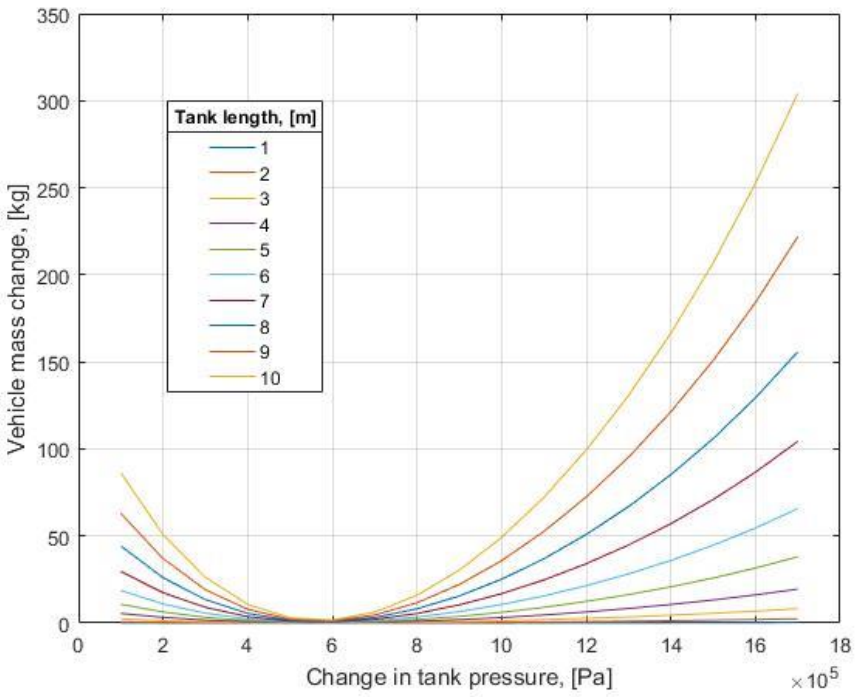

Figure 5-3: Change in vehicle mass as a function of the change in tank pressure (relative to 3 bar) for varying sized vehicles utilizing an electropump system

The mass models were applied to the hypothetical launch vehicle devised in Chapter 2, with the results being given in Figure 5-4. For the turbopump system, an increase in tank pressure results in an increase in vehicle mass thus an inducer is needed to deal with any cavitation at the pump inlet. The electropump system displays an optimal tank pressure at 9 bar, which results in the least vehicle mass gain (the vehicle mass is increased by 0.12 kg).

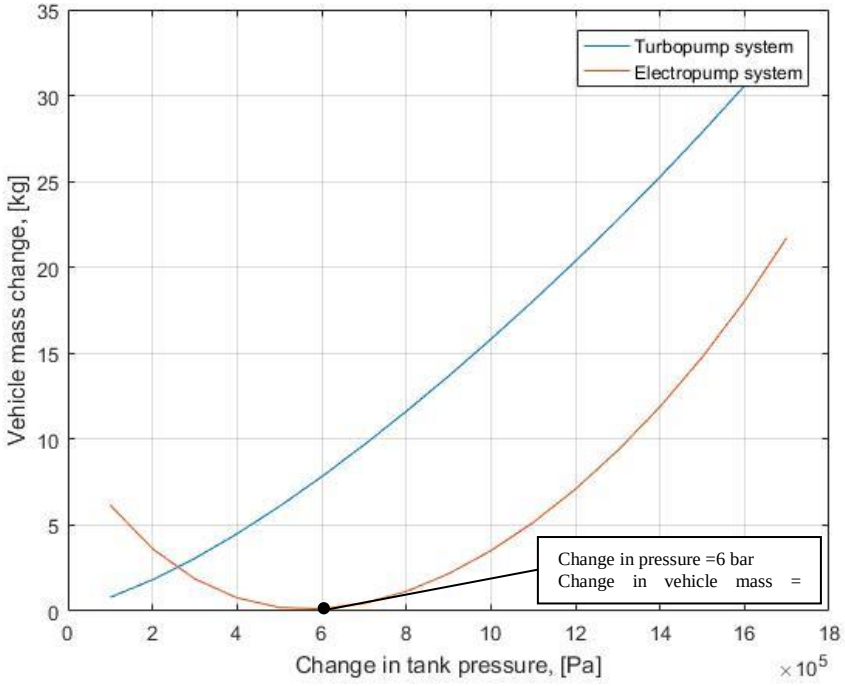

Figure 5-4: Comparison of vehicle mass change for a hypothetical launch vehicle using a turbopump and electropump system

5.3 Analysis of hybrid design with 9 bar inlet pressure

The purpose of this analysis is to ensure that the inlet cavitation on the impeller has been mitigated, and that the pump still satisfies the hydrodynamic requirements of the engine.

When supplied with an inlet pressure of 9 bar, the CFD analysis showed no indications of cavitation. The pump delivers 62.02 bar of pressure with a 62.12 % efficiency. The power required to drive the pump is 28.12 kW, 3.48 kW less than the design using a 3 bar inlet pressure. The static pressure scalar field, absolute velocity vector field and relative velocity vector field can be found in Appendix D, Figures D.1, D.2 and D.3 respectively. Table 5-1 provides a comparison between the hybrid design's performance at a 3 bar and 9 bar inlet pressure.

Table 5-1: Hybrid design performance comparison between 3 bar and 9 bar inlet

	3 bar inlet	**9 bar inlet**
Speed	22300	21250
Delivery pressure	61.8 bar	62.12 bar
Hydraulic efficiency	62.6%	62.12%
Power	31.6 kW	28.12 kW
Radial load	138.6 N	126.3 N

6. Discussion and Conclusion

6.1 Study Objectives

This work began with the development of an RP-1 electropump for a 25 kN, modular liquid rocket engine. The methodology detailing how the engine parameters were obtained, was discussed in Chapter 2. The iterative design process is unavoidable due to the interdependent nature of the isentropic nozzle flow functions and the combustion analysis. The key engine parameters established were the combustion chamber pressure of 50 bar, RP-1 flowrate of 2.75 kg/s (based on a sea level O/F ratio of 2.45) and sea-level specific impulse of 295 s. The hypothetical mission and associated vehicle resulted in a first stage burn time of 116 s.

A mock feed system was created to determine the pump's required delivery pressure. A pressure drop of 20% over the combustion chamber was prescribed for the injector. An algorithm was then written to generate a design from conventional meanline pump theory. The resulting impeller geometry had an excessively small exit width which meant narrow passageways. The dominant frictional losses in the narrow flow domain degraded the pump efficiency. The Barske pump was investigated as an alternative to the conventionally designed pump. The physics defining the principle of operation for the Barske pump was derived from the Navier-Stokes equations.

The fluid domain of each design was drawn with a generic CAD package, whilst STAR CCM+™ was used to analyse the flow fields of each design and compare their respective performances. The Barske pump proved to be superior to the conventional design, based on its higher efficiency potential. The flow field of the Barske design exhibited a significant degree of non-axisymmetry which caused a nett radial thrust of circa 470 N. A hybrid design, consisting of a Barske impeller and scroll collection volute, was generated with the objective of reducing the radial load. The analysed hybrid design produced a nett radial thrust of 167 N. Cavitation was observed at the impeller inlet, which resulted in the CFD analyses being precise but inaccurate. Thus, the simulations are useful for design comparison and optimisation but the quantitative values of efficiency should be treated with caution, due to the lack of multi-phase physics in the steady-state simulation. For the steady-state simulation to yield reliable results, the pressure field should not drop below RP-1's vapour pressure of 2275 Pa.

An investigative case study was performed to assess the best method of mitigating the cavitation. In traditional turbopump design, convention dictates the addition of an inducer. In most cases, this is the optimal solution as increasing tank pressure requires thicker walled pressure vessels, adding undesirable weight to the vehicle. Increased tank pressure reduces the

hydraulic power requirement on the pump, consequently reducing the amount of fuel needed to drive the turbopump. However, due to the high energy density of the fuel, the mass reduction as a result of the fuel saving is less than the additional tank mass. In the electropump case the lithium polymer batteries have about a quarter of the fuel's energy density, thus prompting the investigation into how varying the tank pressure would affect the nett change in vehicle mass. The optimal tank pressure, for the electropump system, was found to be 9 bar. The increased tank pressure eliminated the occurrence of cavitation at the impeller inlet.

The primary objectives of this work were listed in Chapter 1. The first objective was to establish the relevant engine and vehicle parameters that would provide the hydrodynamic requirements of the centrifugal pump. These parameters included the combustion chamber pressure (50 bar), specific impulse (295 s sea-level, 324 s vacuum), propellant mass flow rate (8.64 kg/s), O/F ratio (2.45 sea-level, 2.6 vacuum) and engine burn time (116 s). The second objective was to develop the hydrodynamic design of a centrifugal fuel pump that satisfies the requirements of the engine while simultaneously attempting to minimize the weight and maximize the efficiency. The final pump design operates at a speed of 21250 rpm and discharges RP-1 at a pressure of 62 bar with a flow rate of 2.75 kg/s. The overall pump efficiency is 62.12 %.

6.2 Recommendations for further development

A fluid structural analysis should be done to determine the structural integrity of the generated impeller geometry. The results of the hydrodynamic analysis may be used in a vibrational analysis to ensure the pump does not operate at a critical speed, thus preventing whirling of the rotor which may lead to catastrophic failure of the pump. The mechanical design of the seals, bearings and shaft is required prior to manufacture and physical testing. The actual pump curves may be obtained through physical experimentation and used in an electrical control system to regulate the desired flow rate via motor speed control; a feature which is easier to achieve with electropumps than turbopumps. The introduction of a full cavitation model is advised to more precisely confirm the impact that a cavitation vapour bubble covering parts of the leading edge, would have on overall efficiency.

Further hydrodynamic optimization may be done around the tongue of the volute; this would help reduce the radial load on the impeller by promoting axial symmetry of the pressure field. The radial vanes of the Barske impeller created vortices on the suction side of the blades near the periphery of the impeller, as seen in Figure 6-1. The efficiency of the pump may be improved if these vortices are mitigated. A proposed solution is to curve the blade tips backwards and taper the ends. An iterative CFD optimization process is required to validate the

suggested design change as well as to determine the optimal geometric parameters, that is, flow exit angle, degree of curvature, and so on.

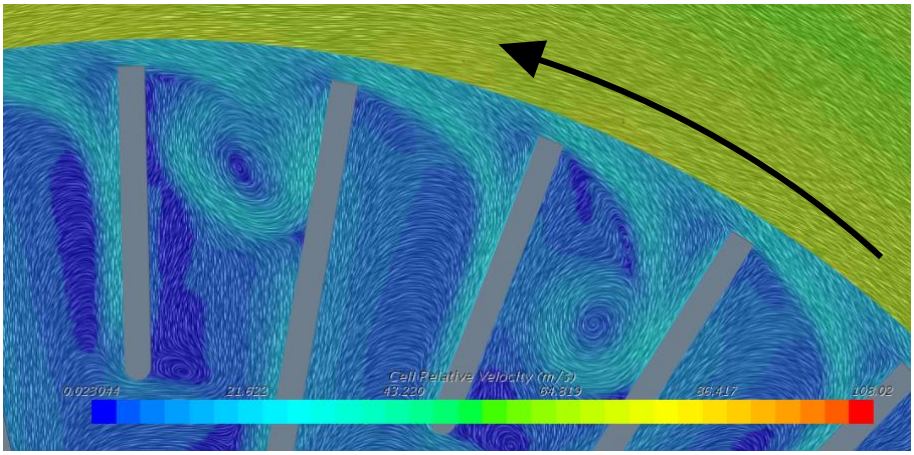

Figure 6-1: Induced trailing vortices by radial blades

References

Balje, O., 1981. *Turbomachines. A guide to design, selection and theory.*. New York: John Wiley and Sons.

Barske, U., 1950. *High Pressure Pumps for Rocket Motors,* Westcott: Royal Aircraft Establishment.

Daily, J. & Nece, R., 1960. *Chamber dimension effects on induced flow and frictional resistance of enclosed rotating disks,* Boston: ASME.

Eckardt, D., 1980. Flow field anaylysis of radial and backswept centrifugal compressor impellers, Part 1: Flow measurements using a laser velocimeter. In: *Performance prediction of centrifugal pumps and impellers.* New york, American Society of Mechanical Engineers.

Fitzgerald, D. J., 2015. *Preliminary Design of a Gas Turbine to Drive a South African Comercial Booster Engine.* Orlando, American Institute for aeronauticas and astronautics Propulsion and Energy .

Gallton, D., 2012. *The challenge of small satellite systems to the space security environment,* Monterey: Naval Postgraduate school.

Gashayija, J. M. & Biermann, E., 2011. Design and devlopment of an image classification and recognition system for cubesat constellation. *International Journal of Computer Applications,* 36(11), pp. 26-30.

Gordon, S. & McBride, B. J., 1994. *Computer Program for Calculation of Complex Chemical Equilibrium Compositions and Applications,* Cleveland: National Aeronautics and Space Administration (NASA).

Gülich, J. F., 2007. *Centrifugal Pumps.* London: Springer Science and Business Media.

Hedi, M. L., Hatem, K. & Ridha, Z., 2012. Numerical Analysis of the Flow Through in Centrifugal Pumps. *International Journal of Thermal Technologies,* 2(4), pp. 216-221.

Hermsen, R., 2017. *Cryogenic propellant tank pressurization,* Delft: Delft University of Technology.

Humble, R., Henry, G. & Larson, W., 1995. *Space Propulsion Analysis and Design. United States of America*: McGraw-Hill.

Huzel, D. K. & Huang, D. H., 1992. *Modern engineering for design of liquid-propellant rocket engines.* Washington: American institute of Aeronautics and Astronautics.

Japikse, D., Marscher, W. D. & Furst, R. B., 2006. *Centrifugal Pump design and Perfomance.* Vermont: Concepts NREC.

Kabir, M., 2000. Finite Element Analysis of Composite Pressure Vessels with a Load Sharing Mettalic Liner, Tehran, *Composite structures*, 49, pp. 247-255

Karassik, I. J., Krutzsch, W. C., Fraser, W. H. & Messina, J. P., 1986. *Pump Handbook.* Singapore: McGraw-Hill.

Li, W.G., 2013. Effects of Flow Rate and Viscosity on Slip Factor of Centrifugal Pump Handling Viscous Oils. *International Journal of Rotating Machinery.*

Lobanoff, V. S. & Ross, R. R., 1992. *Centrifugal Pumps Design and Application*, 2nd edition. Houston: Gulf Publishing Company.

Mao, J. Y., Yuan, S. Q., Pei, J., Zhang, J. F., Wang, W. J., 2014. *Applications of different turbulence models in simulations of a large annular volute-type pump with the diffuser.* Zhenjiang, IOP Conference Series: Earth and Environmental Science.

Martensson, H., Andersson, S., Trollheden, S. & Brodin, S., 2008. Rocket Engines: Turbomachinery. *VOLVO Aero Corporation.*

NASA, 1988. *NSTS Shuttle Reference Manual*, Washington: NASA.

Nemdili, A. & Hellmann, D.-H., 2004. *Development of an empirical equation to predict the disk friction losses of a centrifugal pump.* Timisoura, Romania, The 6th international conference on hydraulic machinary and hydrodynamics.

Ren, Y., Zhu, Z., Wu, D., Mu, J., Li, X., 2016. An improved turbulence model for separation flow in a centrifugal pump. *Advances in Mechanical Engineering, 8(6), pp. 1-10.*

Rocket Lab, 2017. *Electron.* [Online]
Available at: https://www.rocketlabusa.com/latest/

Satoh, H., Uchida, K. & Cao, Y., 2005. *Designing an Ulra-Low Specific Speed Centrifugal Pump.* Tokyo, pp. 16-21.

Schilling, J., 2009. *Launch Vehicle Performance Estimation.* [Online]
Available at: http://silverbirdastronautics.com
[Accessed 5 March 2016].

Schilling, J., 2016. *Delta V split recommendation* [Interview] (13 August 2016).

Singh, N., 2017. *The hydrodynamic design and analysis of a liquid oxygen pump impeller for a rocket engine.* MSc thesis, University of KwaZulu-Natal, Durban.

Smyth, J., 2014. *The design and analysis of a kerosene turbopump for a South African commercial launch vehicle,* MSc thesis, University of KwaZulu-Natal, Durban.

Space Exploration Technologies Corp., 2013. *SpaceX.* [Online]
Available at: http://www.spacex.com/news/2006/01/01/octaweb
[Accessed 4 August 2016].

Sutton, G. P. & Biblarz, O., 2001. *Rocket Propulsion Elements.* New York: John Wiley & Sons..

Tacca, H., 2010. *Electric Feed Systems for Liquid Propellant rocket Engines,* Buenos Aires: University of Buenos Aires.

Tsuei, H.H., 2001. *The role of CFD in turbomachinary designs.* New York, ASME International Mechanical Engineering Congress and Exposition.

Ucer, A. S., 1994. *Introduction and overview to turbomachinary design using CFD.* Turkey: Advisory Group for Aerospace Research and Devlopment.

Westra, R. W., 2008. *Inverse-design and optimazation methods for centrifugal pump impellers,* Enschede: University of Twente.

Wunderlin, N., 2016. *Design of an Ablatively Cooled Combustion Chamber for the SAFFIRE engine.* Annual Conference of the Aeronautical Society of South Africa (AESSA), Pretoria.

Appendix A: Moody Diagram

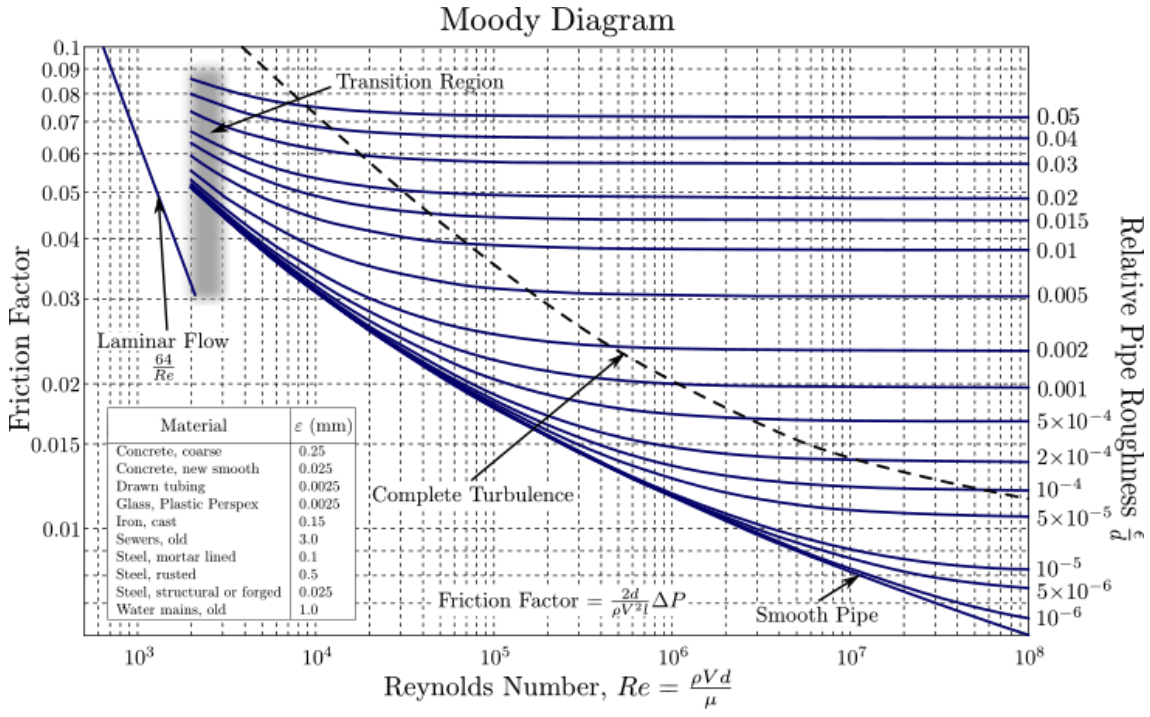

Material	ε (mm)
Concrete, coarse	0.25
Concrete, new smooth	0.025
Drawn tubing	0.0025
Glass, Plastic Perspex	0.0025
Iron, cast	0.15
Sewers, old	3.0
Steel, mortar lined	0.1
Steel, rusted	0.5
Steel, structural or forged	0.025
Water mains, old	1.0

Figure A.1: Moody diagram

Appendix B: Design Algorithms

B.1 Impeller inlet design algorithm

```
clear all

%Inputs
safetyfactor = 1.03;
Required_headrise = 744.7;
Mass_flow_rate = 2.75;
Vapor_pressure = 2275;
Inlet_total_pressure = 3*10^5;
Fluid_density = 819;




g = 9.81;
rho = Fluid_density;
Q = Mass_flow_rate/rho;

mdot = Mass_flow_rate;
sigb = 0.3; %cavitaion coefficient
Pv = Vapor_pressure;
P0 = Inlet_total_pressure*0.9;
Hreq = Required_headrise*safetyfactor;
Tal = 118.9*10^6; %allowable shear stress for 316 stainless steel
shaft_safety_factor = 1.5;
i = 0;
tolerance = 0.1;
err = 5; %initial guess
step = 1;
b1 = 0.005;

%Impeller inlet design

N = 5000;%initial guess
NPSHA = (P0 - Pv)/(rho*g)

while err > tolerance

    i =  i+1

        w = (2*pi*N)/60;
        nq = (N*(Q^0.5))/(Hreq^0.75); %specific speed
        eff = 0.6;
        P = (rho*g*Q*Hreq)/eff;
        r_shaft = ((((16*P)/(pi*w*Tal))^(1/3))/2);
        r1h = r_shaft*shaft_safety_factor;
        r1 = ((r1h^2)+ ((2^(1/3))*((30*Q)/((pi^2)*N))^(2/3)))^0.5;
        r1m = (r1h + r1)/2;
        Cm1 = Q/(0.9*pi*((r1+0.0005)^2 - r1h^2));
        beta1b = (atan(Cm1/(r1m*w)))*(180/pi);
        NPSHR = ((0.5*Cm1^2*(1+sigb) + 0.5*sigb*((r1*w)^2))/g);
        err = abs(NPSHR - (0.7*NPSHA));
```

```
        if i > 10
            i = 0;
            err2 = err;
                if err1 < err2
                    step = step*(-1);

                end
        end

        if err > 10
            N = N+(step*1000);
        elseif err < 1
                N = N+(step*25);
        else
            N = N+(step*50);
        end

        if i == 2
            err1 = err;
        end


end

%outputs
N
nq
eff
r1
r1h
beta1b
```

B.2 Conventional impeller exit design algorithm

```
clear all

%Inputs
rho_tank = 1350; %Tank material density
YS = 1200*(10^6); %Tank material tensile strength
rho_fuel = 819; %Fuel density
SE = 2126.43*(10^3); %Specific energy of fuel
SE2 = 468*(10^3);%Specific energy of lithium polymer battery
AR = 8; %Tank aspect ratio length/radius
k=0;
var=0;
j=0;
g = 0;
mp = 9905.2; %prop mass
OF = 2.45; %O/F ratio

pr = 62*(10^5);
P0 = 3*(10^5);
eff_T = 0.65;
eff_M = 0.9*0.95;
eff1 = 0.62;

for l = 1:1:10

    r = l/AR;
    j = j+1;

    for P = 100000:100000:2000000

        k = k+1;
        Pb = (P/(10^5))+3;
        hydro_eff = - 0.0121*(Pb^3) + 0.3347*(Pb^2) - 2.5403*(Pb)
+67.594; %hydraulic efficiency of hybrid design
        eff_H = hydro_eff/100;

        Z = (rho_tank*l*pi*(r^2))/YS;
        mt1 = Z*(3*P + 2.25*(1/YS)*(P^2));
        mf = ((pi*(r^2)*l)/(SE*eff_T))*(((pr - (P0+P))/eff_H)-((pr-
P0)/eff1));
        mb = ((pi*(r^2)*l)/(SE2*eff_M))*(((pr - (P0+P))/eff_H)-((pr-
P0)/eff1));
        mt2 = (mf*mt1)/(rho_fuel*pi*(r^2)*l);
        m = mt1 + mf + mt2;
        m2 = mt1+ mb;
        marr (k,j) = m;
        marr2 (k,j) = m2;

        if g == 0

        Parr (k,1) = P;

        end
    end
    g =1;
    k = 0;
```

```
end

mfuel = mp/(OF+1);
Vf = mfuel/rho_fuel;
r = (Vf/(pi*AR))^(1/3);
l = AR*r
s = 0;

 for P = 100000:100000:2000000



        s = s+1;
        Pb = (P/(10^5))+3;
        hydro_eff = - 0.0121*(Pb^3) + 0.3347*(Pb^2) - 2.5403*(Pb)
+67.594;
        eff_H = hydro_eff/100;
        Z = (rho_tank*l*pi*(r^2))/YS;
        Mt1 = Z*(3*P + 2.25*(1/YS)*(P^2));
        Mf = ((pi*(r^2)*l)/(SE*eff_T))*(((pr - (P0+P))/eff_H)-((pr-
P0)/eff1));
        Mb = ((pi*(r^2)*l)/(SE2*eff_M))*(((pr - (P0+P))/eff_H)-((pr-
P0)/eff1));
        Mt2 = (mf*mt1)/(rho_fuel*pi*(r^2)*l);
        M = Mt1 + Mf + Mt2;
        M2 = Mt1+ Mb;
        Marr (s,1) = M;
        Marr2 (s,1) = M2;
 end

 %%
figure (1)
plot(Parr,marr)
grid on
lgd =
legend({'1','2','3','4','5','6','7','8','9','10','Location','northwest
'})
title(lgd,'Tank length, [m]')
xlabel('Change in tank pressure, [Pa]')
ylabel('Vehicle mass change, [kg]')

figure (2)
plot (Parr,marr2)
grid on
lgd =
legend({'1','2','3','4','5','6','7','8','9','10','Location','northwest
'})
title(lgd,'Tank length, [m]')
xlabel('Change in tank pressure, [Pa]')
ylabel('Vehicle mass change, [kg]')

figure (3)
plot(Parr,Marr)
hold on
plot(Parr,Marr2)
grid on
legend 'Turbopump system' 'Electropump system'
xlabel('Change in tank pressure, [Pa]')
ylabel('Vehicle mass change, [kg]')
```

Appendix C: CFD Results for Conventional Pump Design with 3 bar Pressure Inlet

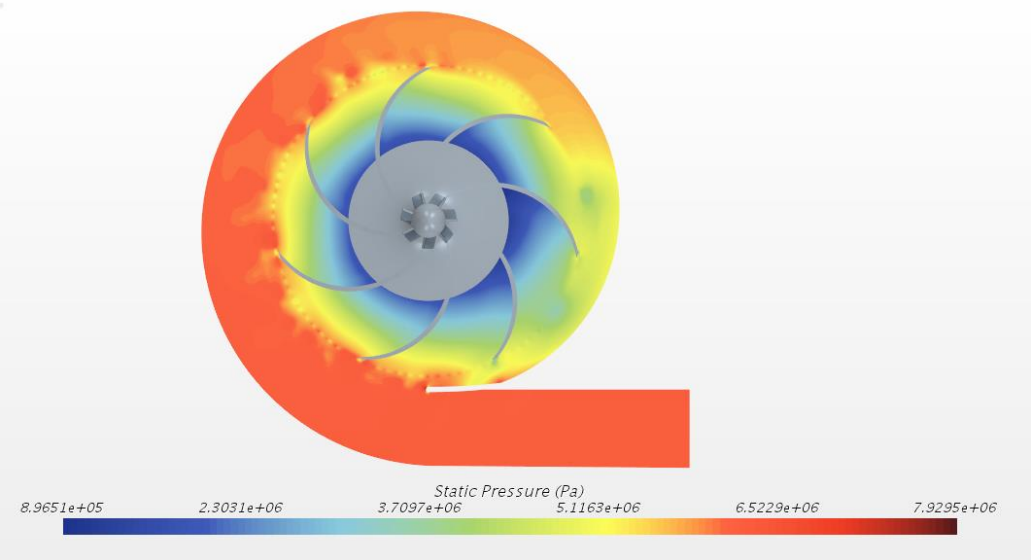

Figure C.1: 2-D cross section of the conventional design static pressure field at 3 bar pressure inlet

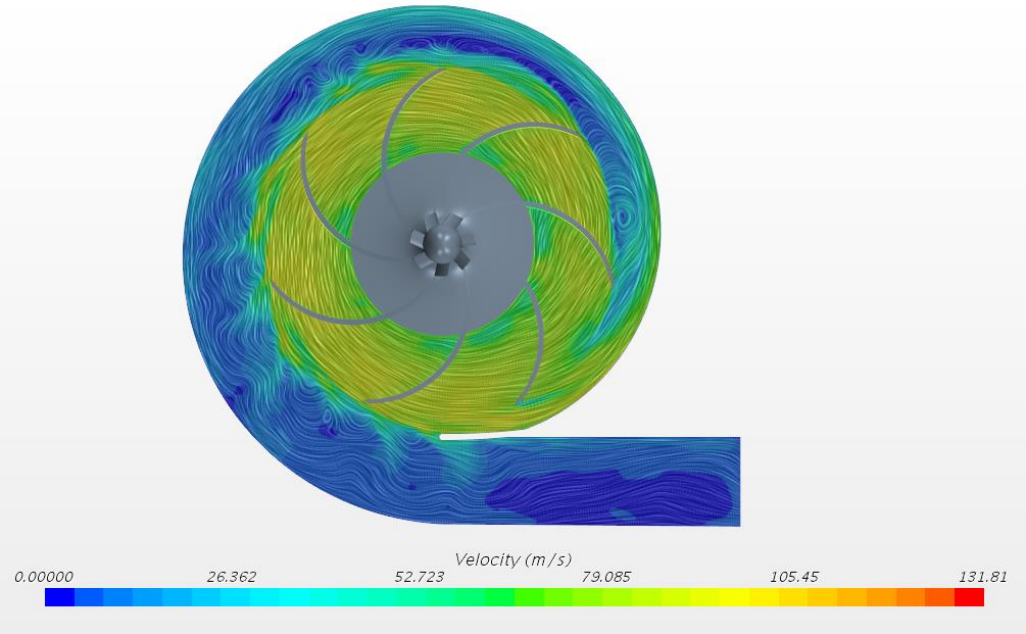

Figure C.2: 2-D cross section of the conventional design absolute velocity vector field at 3 bar pressure inlet

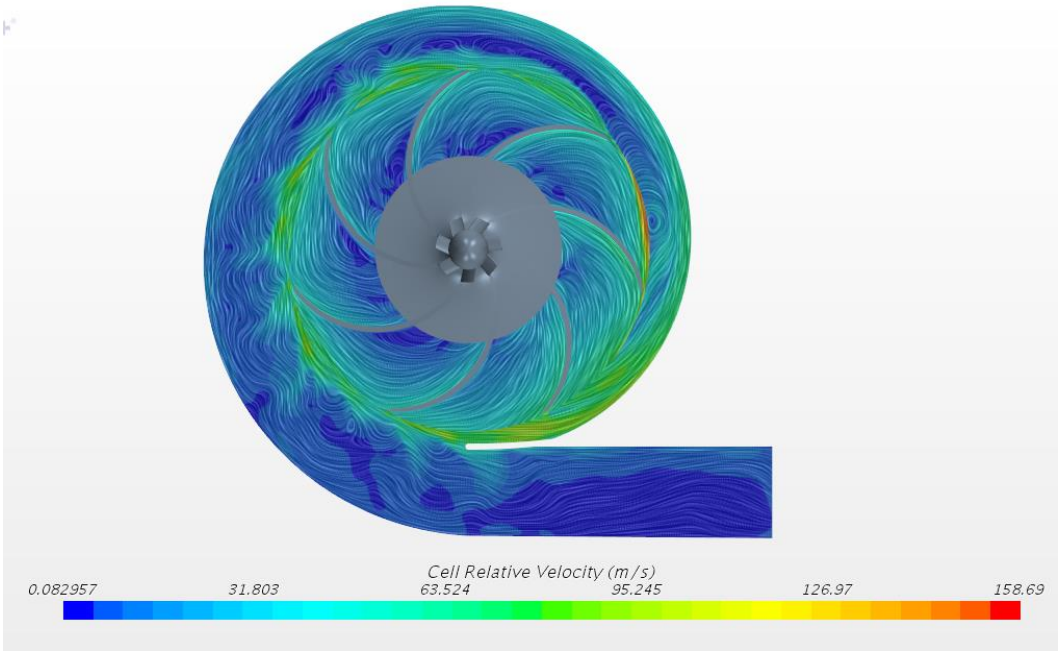

Figure C.3: 2-D cross section of the conventional design relative velocity vector field at 3 bar pressure inlet

Appendix D: CFD results for final hybrid pump design with 9 bar Pressure Inlet

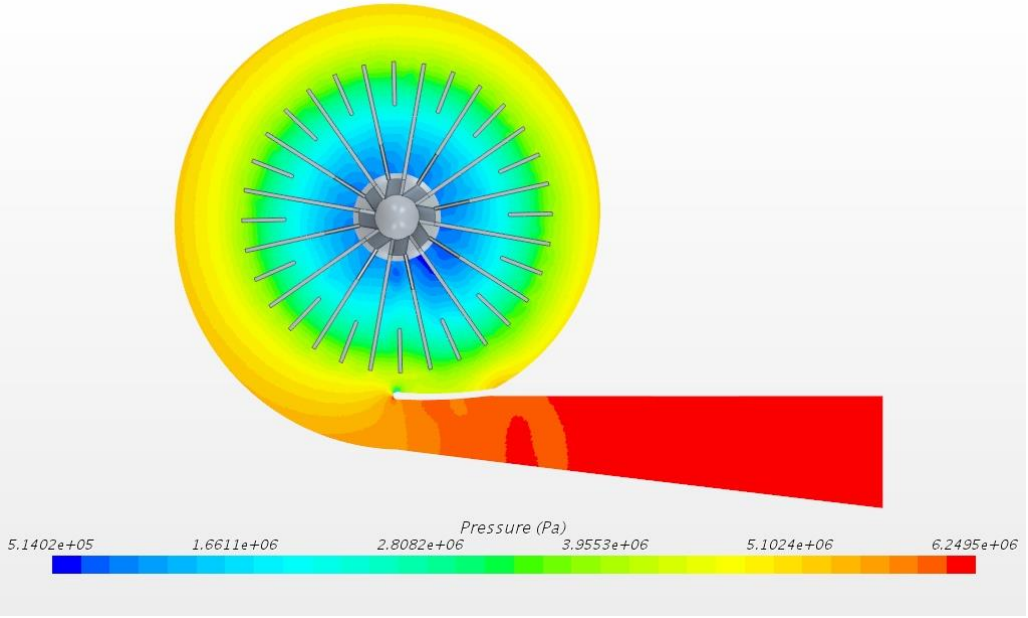

Figure D.1: 2-D cross section of the hybrid design static pressure field at 9 bar inlet pressure

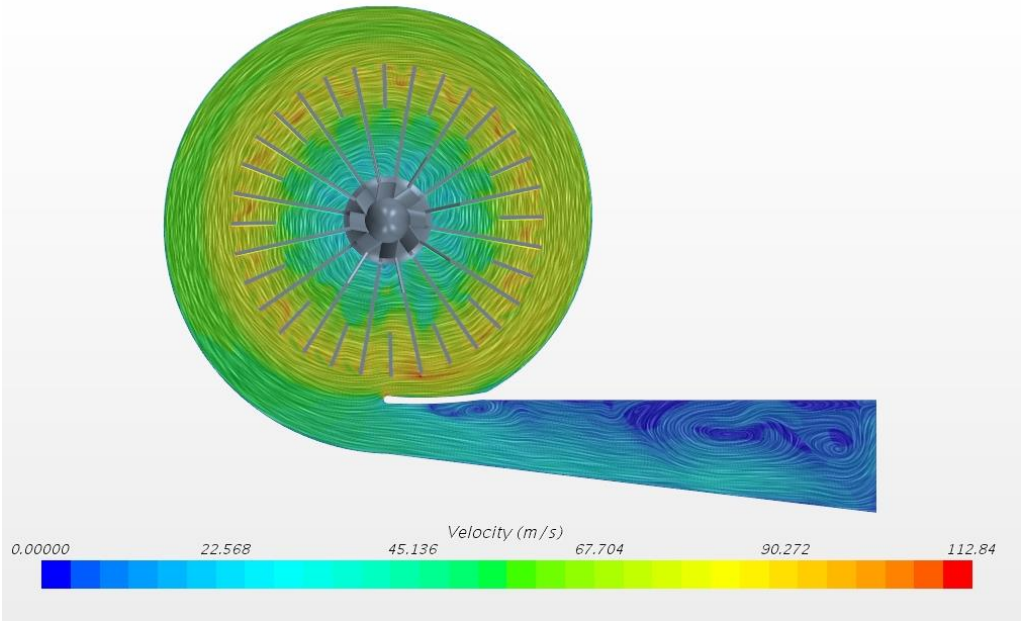

Figure D.2: 2-D cross section of the hybrid design absolute velocity vector field 9 bar inlet pressure

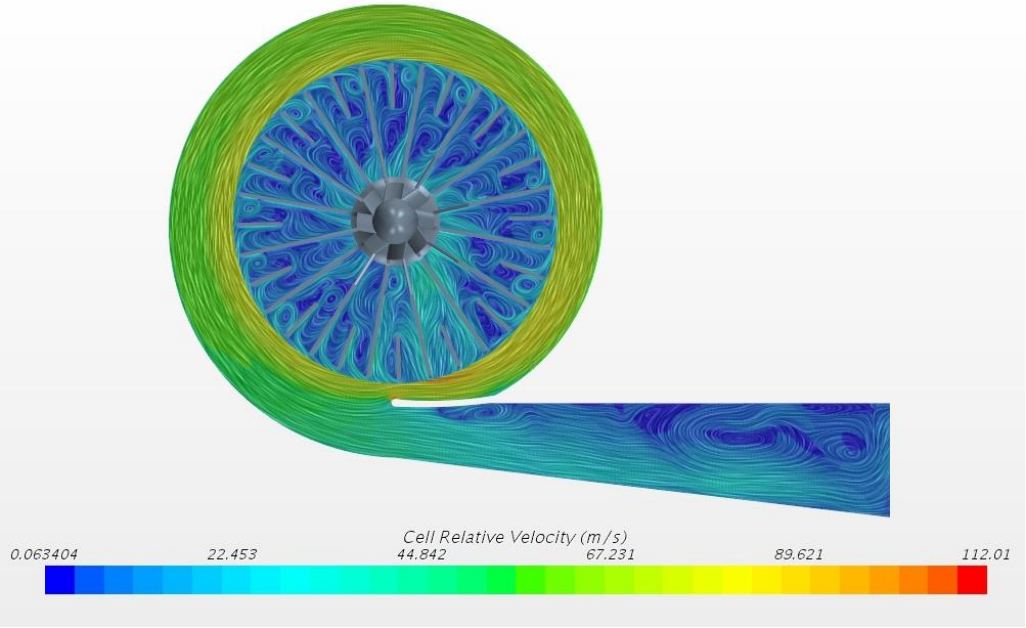

Figure D.3: 2-D cross section of the hybrid design relative velocity vector field 9 bar inlet pressure